UNIVERSITY OF COPENHAGEN
FACULTY OF SCIENCE

„ ,

PhD thesis

Asger J. S. Bolet

Electrohydrodynamics in one– and two–phases

This thesis has been submitted to the PhD School of The Faculty of Science, University of Copenhagen

Advisor: Joachim Mathiesen

Submitted: May 14, 2018

Abstract

Transport of electrolytes in rock–formations, where the fluid paths are on the scale of micrometers down to nanometers, are common in geology. If the rock–electrolyte interface is charged, the effect on flow–permeability can be rather dramatic on such a small scale due to the electric double layer. Good theoretical and numerical studies of such effects have been rather limited because of strong non-linearities of the governing equations, which are even difficult to handle in simple geometries. However, in this work we present a numerical study of geometrical effects on electrohydrodynamic flow in a model fracture, a channel with sinusoidal varying depths. The simulations suggest that electrohydrodynamics leads to increased channeling of the flow which might be of importance in rock precipitation and dissolution.

Furthermore, electrolytes can also play a key role in two-phase flow as it can change the wetting properties on a macroscopic scale, leading to vastly different transport properties. Such electrowetting effects are present near charged rock–fluid–interfaces and play a vital role in settings where two immiscible fluids coexist in a porous media. To study such phenomena in pore–like geometries we have performed a numerical study of two–phase electrohydrodynamics. In these simulations we have seen clear evidence that the release of an electric–inert fluid from a charged pore can be driven by electric–interactions between the pore-wall and the ions of electrolyte.

Resumé

Transport af elektrolytter igenne stenformationer, hvor væske porene er på skalaen af mikrometer ned til nanometer, er almindelige forkommende i geologi. Hvis stenmarterialets overflade er elektrisk ladet, kan effekten på strømningsgennemtrængelighed være temmelig dramatisk på disse små skalaer på grund af det elektriske dobbeltlag. Teoretiske og numeriske undersøgelser af sådanne effekter har været ret begrænsede på grund af stærke ikke-lineariteter af de styrende ligninger, der er vanskelige at håndtere i selv enkle geometrier. I dette arbejde præsenterer vi imidlertid en numerisk undersøgelse af geometriske effekter på elektrohydrodynamisk strømning i en modelfractur, en kanal med sinus varierende dybder. Simuleringerne tyder på, at elektrohydrodynamik fører til øget lokalisering af væskestrømmen, som kan være af betydning for sten-udfældning og opløsning.

Endvidere kan elektrolytter også spille en nøglerolle i to-fase strømning, da det kan ændre vædningsegenskaberne på makroskopisk skala, hvilket kan fører til vidt forskellige transportegenskaber. Sådanne elektrovædningsphenomener er til stede nær ladede sten-væske-grænseflader og spiller en afgørende rolle i situation, hvor to ublandbare væsker sameksisterer i et porøst medium. For at studere sådanne fænomener i porøse geometrier har vi udført en numerisk undersøgelse af to-fase elektrohydrodynamik. I disse simuleringer har vi set klare tegn på, at frigivelsen af en elektrisk-inert-væske fra en ladet pore kan drives af elektriske interaktioner mellem porevæggen og ionerne fra en elektrolyt.

Publication List

Publications by Asger Bolet

Manuscripts published

- Bolet, Asger and Linga, Gaute and Mathiesen, Joachim (2018) Electrohydrodynamic channeling effects in narrow fractures and pores. Physical Review E 97, 043114

Manuscripts under review

- Linga, Gaute and Bolet, Asger and Mathiesen, Joachim (2018) Phase-field modelling of dynamic electrowetting with electrolytes. Physical Review E, preprint ad: http://arxiv.org/abs/1805.01435

Manuscripts in draft form

- Linga, Gaute and Bolet, Asger and Mathiesen, Joachim (2018) Decoupled energy-stable schemes for transient electrohydrodynamic flow.

- Linga, Gaute and Bolet, Asger and Mathiesen, Joachim (2018) BERNAISE: A flexible framework for two-phase electrohydrodynamic flow.

Acknowledgements

I want to thank:
The Villum foundation and the State of Denmark for providing the capital for the project.
The Niels Bohr Institute for giving me an office and a bureaucracy to work within.
Joachim Kaj Matthisen for being both Ph.D. and trip advisor.
Gaute Linga for collaboration both scientifically and as a taco producer.
Florian Uekermann for the help with programming, discussing computers and German politics.
Rastin Matin, Anier Hernandez and Olga Henneberg, for sharing office with me, helping me out in times of need, and having the same interests in boats and planes.
Jens Tarp, Amalie Christensen, Anders Møllgaard, Marek Miztal and Jonas Juul for being good colleagues both at the Institute and at *Sørenes*.
Henrik Bruus, for suggestions and discussion on microfluidics.
The Biocomplexity group for nice lunch discussions on all matters from bacteria to the Carlsberg stock and a nice yearly break dance fight-night a.k.a. The Christmas lunches.
Stephane Santucci, Francois Renard, Christophe Raufaste and Céleste Odier, for their hospitality on different occasions visiting the 5th Republic.
"*Loppen*" For never giving up even if its silicon is getting old and its tasks are getting heavier.
Lars Bolet, Lisbeth Jeppesen, for giving me food when I was less than two meters and sending me to school instead of the lignite quarry.
Sigrid and Olav for helping conquering the world several times during my childhood and the continuing support.
To my other friends for making my remaining weekends and hours less dull and sometimes even fun and memorable.

Contents

List of Figures

List of Tables

Chapter 1

Introduction

1.1 One Phase Electrohydrodynamics

Electrohydrodynamics has a history spanning now over 200 years. The first resisted observation of electric forces affecting fluid motion in a controlled experiment, is attributed to the two scientists Strakhov and Reuss. They observed that dispersed clay particles migrated when placed in an electric field, which today is attributed to (electrockinetics[1]), a phenomenon known as electrophoresis. The observation of a streaming potential was made by Quincke around 1859 in capillary experiments. On the theoretical side early results were provided by Helmholtz (1879), and later Smoluchowski [81, 82] modelled electrophoresis and the streaming potential. At the same time Nernst [55] and Planck [60] were working on the equation that bears their name. The theoretical development continued with the works of Gouy and Chapman introducing the Poisson–Boltzmann equation, a statistical description of the electric double layer, just prior to the Great War. Debye and Hückel used a linearized form of the Poisson-Boltzmann equation by the early twenties [78] which provided the foundation for much of later theoretical estimates. More elaborated models for the electrolyte solid interfaces were further developed throughout the twentieth century to include chemical reactions and high-density corrections, and to allow studies of catalysts and batteries. However, in the context of this work, Verwey and Overbeek's [79] and Rice and Whitehead's [63] solutions of Gouy and Chapman's equations in different settings have been of great importance.

In the more specific context of geophysics, electrokinetic effects have proved to be a tool to measure seismic events [76], and to be able to infer some properties of rocks under influence of seismic waves [46]. Such electroseismic responses were demonstrated to be useful in the exploration of aquifers and monitoring of pollution at shallow to moderate depths under the Earth's surface [75]. Electrokinetic effects associated with seismic activity have also been proposed as a means of earthquake detection [49, 10], and as sources of increased dissipation in water-filled rocks shaken by the seismic activity [61]. The effects of electrokinetics on permeability in artificial porous materials have been studied by network analysis [58] and in experimental settings in various types of stone and ceramic [74].

Although computational studies of electrodynamic effects have a rather long history, these effects in more complicated geometries other than channels and pipes have, however, to our knowledge not been studied by direct calculations, neither analytically nor numerically.

By the late seventies, computers had become so commonly available that numerical solutions of the Poisson-Nernst-Planck problem were possible for the 1-dimensional case [14] and was used for

[1]The terms electrohydrodynamics, electrokinetics and sometimes electro-fluid-dynamics are used more or less synonymously, especially in the early literature.

the studies of ion-exchange membranes [45]. The advances in microprocessors meant that 2- and 3-dimensional Poisson–Nernst–Planck problem simulations were possible around the turn of the millennium [16, 39]. The back coupling to the hydrodynamics leading to Stokes–Poisson–Nernst–Planck problem was considered in two-dimensions by 2005 [44] and in thee-dimensions by 2008 [80]. In both cases this was done with a commercial software, COMSOL, making the numerics somewhat a black-box. However, with the use of FEniCS, an open source software library, Mitscha-Baude et al. [48] were able to implement a solver for the full Poisson-Nernst-Planck problem to study electric effects in cell membranes. This means that studies of flow change in simple nontrivial geometries due to electrohydrodynamic effects should be within the reach of modern computational resources. This will be the subject of Chapter 2 of this work.

1.2 Two Phase Electrohydrodynamics

The electric effects of two-phased electrolytes have been seen as early as 1875 by Lippmann in his electrocapillarity based electrometer [38, 53]. The Lippmann electrometer was due to its sensitivity used for some of the first experimental electrocardiographies(EKG/ECG) done by Waller [84] in the late 1880, but it was soon replaced by more sensitive alternatives.

In a modern context, electrohydrodynamics in two-phase electrolytes has received renewed interest with theoretical as well as experimental work on non-coalescence droplets [64, 52]. But also the increased focus on micro/nanofluidics have sparked renewed interested [72, 68] as electrowetting can be used to control and manipulate small volume of fluids fast and precisely [53, 54].

For other applications, there might be some prospects in the generation of blue energy [71] and in the continued development of electronic ink used in displays [11, 12, 23, 20]. Furthermore, effects of electrohydrodynamic has been exploited in petrochemical recovery where the flooding of a reservoir by so-called "smart water" (petrochemical lingo for a dilute ion-solution), gives increased yield [62]. The effect of smart water have been studied on a laboratory scale and have shown to change the wetting properties of the rock surface [19, 21].

Different models for electrowetting have been proposed over the years, the early models were established by Taylor and Melcher for a leaky Dielectric [73, 47]. However, the leaky dielectric assumption is not valid in the limit where the Debye length is comparable to the droplet size and if the electric field is weak [67].

Recent developments in models have taken the effects of the electrolytes directly into consideration so they are now valid on small-scale droplets [50, 51] Further simulations of droplet deformation in electric fields have successfully been carried out by Yang et al. [85, 86], and some effects of electrowetting were studied by numerical means in the setting of microfluidic devices by Walker et al. [83]

Two-phase flow can be modelled with different approaches, one being sharp–interface models, another is diffuse–interface models. In our case we have used a diffuse–interface model, as this type of model avoids the explicit tracking of the interface. Furthermore, with the model used the phase field equations that do the implicit tracking of the phase can with relative ease be solved within a finite element framework, as used in our studies.

For the history of phase field for two-phase flow, see the review by Anderson et al.[8]. The phase field model for electrolytes continued herein was developed on top of a thermodynamical consistent version of Hohenberg et al.'s H-model [22] by Lowengrub et al. [43]. This model was further improved with a divergent free velocity field by Abels et al.[1], before it reached its final form including electrolytes in a thermodynamical consistency, through the Onsager variational principle due to the

work of Campillo-Funollet et al. [15]

The field of work to which we have contributed is mainly the numerical implementation of the model by Camillo-Funollet et al. and qualitative study of electrowetting in different complex geometries. These studies will be presented in Chapter 3 of this work.

Chapter 2

One Phase Electrohydrodynamics

To give an outline of the present chapter we will begin by motivating the importance of one-phase electrohydrodynamics and then continue in the second section with an introduction to the theoretical background of electrohydrodynamics and some important analytical results. In the third section we discuss numerical methods for solving the introduced equations, along with the problem of mesh generation. Finally, in the last section we present the results of our simulations and discuss what can be done in order to make further progress. This work has also been published in "Electrohydrodynamics channeling effects in narrow fractures and pores" found in Appendix A. Further the time dependent scheme used for bench marking the code in "Electrohydrodynamics channeling effects in narrow fractures and pores" have been drafted into a paper called: "Decoupled energy-stable schemes for transient electrohydrodynamic flow" and can be found in Appendix C.

2.1 Motivation

Electrohydrodynamics can be important in situations involving fluids containing dissolved ions. Especially in confined conditions like a micro-porous sample electrohydrodynamics is likely to become a controlling phenomenon. Micro-porous conditions are routinely found in a number of industrial and natural occurring situations. Such situations are: Purification of water, especially desalination, which can be done by pushing the fluid through a porous ion-selective membrane working by electrostatic repulsion of ions. Fluid-filled porous rocks both in the situation of transport, and in the dissipation of energy during earthquakes [61] or similar events. Furthermore, electrohydrodynamics is also relevant in the petrochemical recovery industries, as flow resistances is important for determining porosity and thereby determining the nature of a reservoir [77]. Finally, water transport in underground settings, like ground-water flow, water saturated rocks and oil wells are as porous settings typically also associated with some dissolved ions.

The effects of surface charge on ion-solutions have been studied in many cases over the years. The studies regard the effects on flowrates of fluids in tubes [63, 61], the effects on charge transport [57], and the effects on generated electric potential in tubes [44].

Our scope is however to investigate the effects on flowrates in porous samples rather than in tubes via computational methods, as this is beyond what can be achived from an analytical approach. The end goal, if possible, would be to establish some sort of simple Darcy' law like relation for electric-kinetic flow.

2.2 Theory

In order to discuss the results of simulating electrohydrodynamics we will need a theoretical understanding of the system. Therefore, we will in this section introduce the equations used to model the electrolyte and the boundary conditions found in physical settings. Furthermore, we will introduce a way to make the equations dimensionless and in addition give some well-known analytical results relating to the electro-viscous effect.

Let us be begin with the models for electrohydrodynamics.

2.2.1 The Governing Equations of Electrohydrodynamics

The three sets of equations that form the foundation of electrohydrodynamics (EHD) are the Navier-Stokes equations for fluid dynamics, the Poisson equation for an electric field and the Nernst-Planck equation for the ion number density. In the following sections, we introduce these equations, their origin, relevant boundary conditions, dimensionless forms and approximate forms in relevant regimes. We will start with the Nernst-Planck equation.

The Nernst-Planck Equation

Let us start with a standard derivation of the Nernst-Planck equation based on phenomenology Fick's law approach [1] and then discuss its shortcomings afterwards. Consider the continuity equation for a number-density of ions in some solution:

$$\nabla \cdot \mathbf{J}_i + \frac{\partial n_i}{\partial t} = 0, \tag{2.2.1}$$

where $\mathbf{J}_i$ is the total number-current-density of the i ion species and n_i is the number-density[2] of the i ion species.

Now if some flow field is imposted on the solution, one will have an advective contribution to the current of the form:

$$\mathbf{J}_i^{ad} = n_i \mathbf{u}, \tag{2.2.2}$$

where $\mathbf{u}$ is the advection velocity or more specific the velocity of fluid.

However, if the number-density is not homogeneous in space or the system is exposed to an external electric field one must consider a diffusion-migration term due to an in-homogeneous electrochemical-potential. Such a term would have the following form:

$$\mathbf{J}_i^{md} = +\lambda_i n_i \mathbf{F}_i, \tag{2.2.3}$$

where λ_i is the mobility of the ions and $\mathbf{F}_i$ is the electrochemical-forces acting on the ions. $\mathbf{F}_i$ is given as:

$$\mathbf{F}_i = -\nabla \mu_i(\mathbf{r}), \tag{2.2.4}$$

where $\mu_i(\mathbf{r})$ is the electrochemical potential for a diluted ion-solution and is given as:

$$\mu_i(\mathbf{r}) = \mu_i^0 + k_b T \ln n_i(\mathbf{r}) + z_i q_e \varphi(\mathbf{r}). \tag{2.2.5}$$

[1] The original derivation can be found in [55, 60].

[2] In chemistry it is normal to use concentration in favor of number-density

Here μ_i^0 is the equilibrium chemical potential, k_b is the Boltzmann constant, T is the temperature, z_i is the valency meaning the relative charge compared to q_e the electron charge [3], and finally, φ is the electric potential.

Now calculating $\mathbf{J}_i^{md}$ explicitly by using Eqs. (2.2.4) and (2.2.5) in conjunction with Eq. (2.2.3) one gets:

$$\begin{aligned}\mathbf{J}_i^{md} &= -\lambda_i k_b T \nabla n_i - \lambda_i z_i q_e n_i \nabla\varphi \\ &= -D_i \nabla n_i - \frac{D_i z_i q_e}{k_b T} n_i \nabla\varphi\end{aligned} \tag{2.2.6}$$

where D_i is defined by the second equality and is the thermal mobility.

Finally, we arrive at the Nernst Planck equation by identifying the total number-current-density as the sum of $\mathbf{J}_i^{md}$ and $\mathbf{J}_i^{ad}$ and plugging it into Eq. (2.2.1):

$$\frac{\partial n_i}{\partial t} = \nabla \cdot \left(-n_i \mathbf{u} + D_i \nabla n_i + \frac{D_i z_i q_e}{k_b T} n_i \nabla\varphi \right) \tag{2.2.7}$$

Note that the term $-\nabla\varphi$ is some times exchanged with its gauge invariant form $-\nabla\varphi - \frac{\partial \mathbf{A}}{\partial t}$. This is in principle fine, but one should be aware that any direct effects of magnetic-fields is still not present. How to introduce such direct effects of magnetic-fields in the Nernst-Planck equation is beyond the scope of this text, but it should be safe to ignore them.

From the number-densities and the number-current-densities of the Nernst-Planck equation one can define the charge-densities and charge-current-density. The charge density is given by the following sum:

$$\rho_e = q_e \sum_{i=1}^{N} z_i n_i, \tag{2.2.8}$$

where N is the number of ion-species. Likewise, the charge-current-density is defined as:

$$\mathbf{J}_e = \sum_{i=1}^{N} z_i \mathbf{J}_i, \tag{2.2.9}$$

With those derivate quantities let us turn to the equation that governs the electric-potential.

The Poisson Equation

In principal one can derive the full Maxwell equations and thereby an equation for electric-potential from first principal along the lines given in [7]. However, as we are not in need of full electrodynamics, we will simply start our treatment of the Poisson equation from the Gauss law as found in [30, 24]. The Gauss law states a relation between the charge-density and the electric-displacement-field in the following manner:

$$\nabla \cdot \mathbf{D} = \rho_e \tag{2.2.10}$$

where $\mathbf{D}$ is know as the electric-displacement-field.

[3] Normally in chemistry lingo the valency is only the absolute value of our definition, however we have expressed it this way in order not to carry an extra parameter just for the sign.

This equation simplifies in the context of a linear-dialectic media as here to the following linear relation between the electric-displacement-field and the electric-field:

$$\mathbf{D} = \epsilon_r \epsilon_0 \mathbf{E} \tag{2.2.11}$$

where ϵ_0 is the vacuum permittivity and ϵ_r is relative permittivity.

In the case of a none-space-dependent relative permittivity, which is typically the case in one-phase electrohydrodynamics, one can rewrite Eqs. (2.2.10) and (2.2.11) as[4]:

$$\nabla^2 \varphi = -\frac{\rho_e}{\epsilon_r \epsilon_0}, \tag{2.2.12}$$

where we have introduced that $\mathbf{E} = -\nabla\varphi$. It should be noted that we have ignored the Faraday law of induction in the definition of the electric field, but that should hardly be a surprise after the discussion in the section of the Nernst-Planck equation.

With an equation for the electric-potential, the only remaining thing we need in order to close the system of equations is to have a way to find the electrolytes velocity field. Here we are going to use the Navier-Stokes equation with a prober force term.

The Navier-Stokes Equation

The Navier-Stokes equation are normally derived from the continuum hypotheses which strictly speaking is a phenomenological approach. Such a derivation can be found in [34, 32]. However, one can also derive the Navier-Stokes equation from a microscopic approach using the Boltzmann equation. This is mainly interesting from a theoretical point of view as it is much more cumbersome than the phenomenological and gives no real advantages such as direct calculation of the model parameters – at best one gets that the parameters depend on temperature. A kinetic derivation of the incompressible Navier-Stokes equation can be found in [9].

Without further to say on the derivation, let us state the incompressible Navier-Stokes equations:

$$\rho\left(\frac{\partial \mathbf{u}}{\partial} + \mathbf{u}\cdot\nabla\mathbf{u}\right) = -\nabla P + \mu\nabla^2\mathbf{u} + \mathbf{F}, \tag{2.2.13}$$

$$\nabla\cdot\mathbf{u} = 0 \tag{2.2.14}$$

where the first equation is the momentum continuity equation and the second is the incompressibility statement. ρ is the fluids mass-density, P is the pressure, μ is the dynamical viscosity and $\mathbf{F}$ is an external force. The force explicitly in mind is the electro-static force on a charge-density in a nontrivial electric-potential:

$$\mathbf{F} = -\rho_e \nabla\varphi \tag{2.2.15}$$

Of course, one can imagine other contributions to the force e.g. gravitation, but as we are planning on applying the equations on a micrometer scale it should be fine to leave such contributions out as the Galilei number is small under these circumstances.

With this closed system of the equations we can now turn to the boundary conditions we will need in order to solve them in realistic conditions.

[4]Note that relative permittivity of a specific substance may typically depend on the density and temperature. As we are interested in rather diluted water-ion solutions and as water can be considered to be incompressible, we have chosen not to consider variation of the temperature at all. A further elaboration on the subject can be found in [61].

2.2.2 Boundary Conditions

Boundary conditions are rather important for the structure of solutions to a partial differential equation especially in confined spaces. This means that boundary conditions should be chosen with care and in such a way that they are consistent the physical situation they are trying to describe. As we have three equations to discuss we will take their boundary condition one at a time.

Let us start with the Nernst-Planck equation. Here we would like to introduce two different boundary conditions: A no-flux condition and a number-density condition. We will consider with the latter first as it is straight forward to formulate as a Dirichlet boundary condition:

$$n_i(\mathbf{x}) = n_i^{\infty}(\mathbf{x});\ \mathbf{x} \in \Gamma_O \tag{2.2.16}$$

where n_i^{∞} is the number-density of the i-ion at an open boundary given by the set Γ_O. The using of a number-density condition is to model the contact with bulk systems of the solution with a specific ion number-density. In conjunction with the number-density at an open boundary it is important to note that charge density given Eq. (2.2.8) should be consistent with the imposed boundary condition of the Poisson equation see Eqs. (2.2.20) and (2.2.21).

Moving on to the no-flux condition which is used to mimic the case of a chemical no-reacting channel wall. In a formal manner it is written as:

$$\mathbf{J}_i(\mathbf{x}) \cdot \mathbf{n}(\mathbf{x}) = 0;\ \mathbf{x} \in \Gamma_S, \tag{2.2.17}$$

where, $\mathbf{n}$ is the surface normal and Γ_S is the set of solid surface e.g. a channel wall. Using the expressions for the number-current-density found in Eqs. (2.2.2) and (2.2.6) and anticipating the no-slip condition on the velocity one gets the following:

$$D_i \nabla n_i(\mathbf{x}) \cdot \mathbf{n}(\mathbf{x}) + \frac{D_i z_i q_e}{k_b T} n_i(\mathbf{x}) \nabla \varphi(\mathbf{x}) \cdot \mathbf{n}(\mathbf{x}) = 0;\ \mathbf{x} \in \Gamma_S \tag{2.2.18}$$

This is the final form of the no-flux condition for the Nernst-Planck equation. We will however make a slight return after we have discussed the boundary conditions of the Poisson equation.

For the Poisson equation we will also consider two types of boundaries: A fixed potential and a surface charge condition. Let us begin with the constant fixed potential condition which we will mainly use for choosing a gauge for the electric-potential and which is having the following Dirichlet typed condition [5]:

$$\varphi(\mathbf{x}) = \varphi_{\Gamma}(\mathbf{x});\ \mathbf{x} \in \Gamma_G, \tag{2.2.19}$$

where φ_{Γ} is the potential on the boundary given by the set Γ_G.

The surface charge condition takes the form of a Neumann condition and is typical written as:

$$\nabla \varphi(\mathbf{x}) \cdot \mathbf{n} = \frac{\sigma_e(\mathbf{x})}{\epsilon_r \epsilon_0};\ \mathbf{x} \in \Gamma_{CW}, \tag{2.2.20}$$

where σ_e is the surface charge density of the wall and Γ_{CW} is the domain of the boundary where the condition is imposed. Note that this condition is not only used for walls but also for open boundaries where one wants to set the normal component of electric-field to zero.

[5] Note that one can also use the fixed potential to specify the so called ζ-potental at a charged-wall ionic-solution interface. However, one will have to be careful when doing this as the concept of a ζ-potental is tied to the Poisson-Boltzmann equation which is a strictly equilibrium equation. Therefore it is not in general valid to impose a ζ-potental in a non-equilibrium situation so in the context of transport one has to use the corresponding surface charge. The concept of the ζ-potental will be revisited and properly explained in Section 2.2.4 under "The Grahame equation".

In addition we can also use Eq. (2.2.20) to specify the no-flux condition of the Nernst-Planck equation a bit more in the situation where Γ_S and Γ_{CW} coincidences, in which case Eq. (2.2.18) becomes:

$$D_i \nabla n_i(\mathbf{x}) \cdot \mathbf{n}(\mathbf{x}) + \frac{D_i z_i q_e}{k_b T} n_i(\mathbf{x}) \frac{\sigma_e(\mathbf{x})}{\epsilon_r \epsilon_0} = 0;\ \mathbf{x} \in \Gamma_S \cap \Gamma_{CW} \tag{2.2.21}$$

Note that we are considering the case where $\Gamma_S \subseteq \Gamma_{CW}$, so Eq. (2.2.21) is the form of the no-flux condition we are going to use.

Finally, we will introduce the boundary conditions for the fluid system. Again we will have two types: A Neumann condition that specifies a pressure boundary and a Dirichlet condition for imposing a velocity at a boundary.

The Dirichlet condition is stated as:

$$\mathbf{u}(\mathbf{x}) = \mathbf{u}_\Gamma(\mathbf{x});\ \mathbf{x} \in \Gamma_V, \tag{2.2.22}$$

where $\mathbf{u}_\Gamma(\mathbf{x})$ is the velocity on the boundaries in Γ_V. This boundary condition of course reduces to the no-slip condition if $\mathbf{u}_\Gamma(\mathbf{x})$ is the zero vector. This special case is normally used to model a solid-fluid interface and it is so important that it will have its own equation:

$$\mathbf{u}(\mathbf{x}) = \mathbf{0};\ \mathbf{x} \in \Gamma_W, \tag{2.2.23}$$

where Γ_W is the path of Γ_V that is a solid-fluid interface. It should be noted that the no-slip condition for some interface material is violated on nanometer scales, however we have considered scales larger than this so we have ignored the phenomenon. [6]. The Neumann condition for a pressure boundary is given as:

$$\nabla \mathbf{u}(\mathbf{x}) \cdot \mathbf{n}(\mathbf{x}) + P\mathbf{n}(\mathbf{x}) = \mathbf{g}(\mathbf{x});\ \mathbf{x} \in \Gamma_I \tag{2.2.24}$$

where $\mathbf{g}$ is some surface force to be applied at the boundary and Γ_I is the set of open boundaries.

After this introduction to the boundary conditions for the different equations we will continue by considering the dimensionless equations and an approximation.

2.2.3 Dimensionless Equations

In this section we will present the dimensionless form of the equations given in Section 2.2.1. But before introducing the non-dimensional equations we will approximate the Navier-Stokes equation in the limit of vanishing Reynolds numbers.

As the Reynolds number is the ratio between the convection term divided by the diffusion term one can ignore the non-linear convection term if the Reynolds number vanishes. To get an idea of the Reynolds number in as specific case it is given as [34]:

$$\mathrm{Re} = \frac{\rho u R}{\mu}, \tag{2.2.25}$$

where u is the fluid speed and R is the characteristic length of the system.

In the case we want to consider, i.e. water flow in channels on nanometer to micrometer scale and low fluid speed in the order of maximum centimeter second, the Reynolds number is never larger that

[6] For some introduction to slip effects on nanometer scales see [56].

Variable	Symbol	Normalization
Ion-number-density	n_i	n^∞
Electric-potential	φ	$V_T = \frac{k_b T}{\bar{z} q_e}$
Length	x	R
Velocity	$\mathbf{u}$	$U_0 = \frac{\epsilon_0 \epsilon_r V_T^2}{\mu R}$
Time	t	$\frac{R^2}{\bar{D}}$
Pressure	P	$\frac{\mu U_0}{R}$

Table 2.1: The tree columns are from left to right: The name of the variable in question, its symbol in the above discussed section and finally the normalization that is used to make the given quantity dimensionless. Note that $\bar{z} = \frac{1}{N}\sum_{i=1}^{N} |z_i|$, $\bar{D} = \frac{1}{N}\sum_{i=1}^{N} D_i$ and n^∞ is chosen to be one of the ion-spices inlet number-density

0.1. Without the convection term the Navier-Stokes equation is known as the time-dependent Stokes equation:

$$me\rho \frac{\partial \mathbf{u}}{\partial t} = -\nabla P + \mu \nabla^2 \mathbf{u} + \mathbf{F}, \tag{2.2.26}$$

and the mass-continuity equation is still on the form given in Eq. (2.2.14).

As we have carried out our approximation, let us turn to the dimensionless equations. The equations will be scaled by following the convention outlined in Table 2.1[18]. Applying the chosen scaling to the Nernst-Planck equation, Eq. (2.2.7), gives the following:

$$\frac{\partial \tilde{n}_i}{\partial \tilde{t}} = \tilde{\nabla} \cdot \left(-\frac{1}{\mathrm{Pe}} \tilde{n}_i \tilde{\mathbf{u}} + \tilde{D}_i \tilde{\nabla} \tilde{n}_i + \tilde{D}_i \tilde{z}_i \tilde{n}_i \tilde{\nabla} \tilde{\varphi} \right), \tag{2.2.27}$$

where the tilde denotes that the quantities are made dimensionless through the scalings given in Table 2.1 and where Pe is the Péclet number describing the ratio between advective and diffusive transport and defines as [7]:

$$\mathrm{Pe} = \frac{R U_0}{\bar{D}}, \tag{2.2.28}$$

The charge density, Eq. (2.2.8), simplifies to:

$$\tilde{\rho}_e = \sum_{i=1}^{N} \tilde{z}_i \tilde{n}_i. \tag{2.2.29}$$

The Poisson equation, Eq. (2.2.12), along with the just stated dimensionless charge density, becomes:

$$\tilde{\nabla}^2 \tilde{\varphi} = -\frac{R^2}{2\lambda_D^2} \tilde{\rho}_e, \tag{2.2.30}$$

where λ_D is the Debye length and is defined as:

$$\lambda_D = \sqrt{\frac{k_B T \epsilon_0 \epsilon_r}{2 \bar{z}^2 q_e^2 n^\infty}}, \tag{2.2.31}$$

[7]Note, that we mostly consider cases where $\tilde{D}_i$ equals 1 and $\tilde{z}_i$ reduces to $\mathrm{sgn}(z_i)$ as this is the case of a symmetric two species ion-solution.

A precise discussion of the physical meaning of the Debye length is postponed until Section 2.2.4 after the introduction of the linearized Poisson-Boltzmann equation Eq. (2.2.48), but for now it is sufficient to know that it is the length scale to expect departure for electro-neutrality near a charged interface.

Finally we have Stokes equation, Eq. (2.2.26), in its dimensionless form:

$$\frac{1}{\mathrm{Sc}}\frac{\partial \tilde{\mathbf{u}}}{\partial \tilde{t}} = -\tilde{\nabla}\tilde{P} + \tilde{\nabla}^2\tilde{\mathbf{u}} + \frac{R^2}{2\lambda_D^2}\tilde{\rho}_e\tilde{\nabla}\tilde{\varphi}, \tag{2.2.32}$$

where the Sc is the Schmidt number defined as:

$$\mathrm{Sc} = \frac{\mu}{\rho \bar{D}}, \tag{2.2.33}$$

and describing the ratio between viscous diffusion and mass diffusion of the ions. Note that the Schmidt number have not been of big impotence in our studies as we have been concerning steady state solutions, but it relates to the time scale where a steady flow is obtained while the ions-number-densities are steady. This means that for a Schmidt number smaller than one the ion-number-densities will equilibrate faster than the flow, while for a Schmidt number larger that one the ion-number-densities will have a longer transient.

For completion we also state the dimensionless form of the fluid mass continuity equation, Eq. (2.2.14), which is:

$$\tilde{\nabla} \cdot \tilde{\mathbf{u}} = 0. \tag{2.2.34}$$

With the dimensionless equations covered we will now turn to introducing some theoretical results in the equilibrium of the Poisson-Nernst-Planck coupled problem. We will furthermore discuss the departure from equilibrium by introducing a non-zero velocity field, where we will be especial interested in the phenomenology of the steady-state.

2.2.4 Statistical Treatment of The Ion-solution

As the coupling between the Poisson equation and the Nernst-Planck equation is strongly non-linear it is challenging to solve even in the simplest of cases. However, in the regime where the electrolyte is at rest, one can turn to a statistical equilibrium approach in order to get an ansatz on the ion number densities that eliminates the Nernst-Planck equation in favor of the Poisson-Boltzmann equation [78]. Furthermore one can get some reasonable results in steady state for simple geometries from such calculation [63].

Starting with the result within equilibrium we will derive the Poisson-Boltzmann equation in detail and then move on with that as a vantage point.

Let us begin by considering the ions as being Boltzmann distributed, i.e. we consider them being in a thermodynamical equilibrium. This means that their momentum follows a Maxwellian distribution if they are otherwise only affected by a classical potential field that acts on the ions center off mass and more important the ions number-density follows the Boltzmann formula [31]:

$$n_i(\mathbf{x}) = n_i^{\infty} \exp\left(-\frac{U_i(\mathbf{x})}{k_B T}\right), \tag{2.2.35}$$

where $U_i(\mathbf{x})$ us the external potential experienced by the i'ed type of ions. Now, if the n_i^{∞} is so small that the mean distance of the ions are large than $(z_i q_e)^2/(\epsilon_r \epsilon_0 k_b T)$[8][28] one can approximate the

[8]For water at room temperature and monovalent ions the distance is $\sim 10\mathrm{nm}$ corresponding to number-densities of $\sim 10^{25}\mathrm{m}^{-3}$

external potential by only considering the electric-potential [9]:

$$U_i(\mathbf{x}) = z_i q_e \varphi(\mathbf{x}) \tag{2.2.36}$$

Introducing Eq. (2.2.36) into Eq. (2.2.35) gives the distribution:

$$n_i(\mathbf{x}) = n_i^\infty \exp\left(-\frac{z_i q_e \varphi(\mathbf{x})}{k_B T}\right), \tag{2.2.37}$$

One could continue in calculating the charge-density via Eq. (2.2.8) and by introducing it to the Poisson equation, Eq. (2.2.12), and end up with a none-linear source term. Instead of pursuing the general case we will, however, consider a symmetric monovalent two species ion-solution which yields to the conventional form of the Poisson-Boltzmann equation, as it allows us to get some derived relations on closed form.

The number-densities in monovalent case is given as:

$$n_\pm(\mathbf{x}) = n^\infty \exp\left(\mp\frac{|z_\pm| q_e \varphi(\mathbf{x})}{k_B T}\right), \tag{2.2.38}$$

where $n_\pm$ is the number-density for the positive and the negative ions respectively and where $n_-^\infty = n_+^\infty = n^\infty$[10].

Introducing Eq. (2.2.38) to Eq. (2.2.12) via Eq. (2.2.8) we arrive at the Poisson-Boltzmann equation:

$$\nabla^2 \varphi = \frac{2 q_e n^\infty}{\epsilon_r \epsilon_0} \sinh\left(\frac{q_e \varphi}{k_B T}\right), \tag{2.2.39}$$

Having established such a nice form of the Boltzmann equation we will derive some results.

The Grahame Equation

First we will consider the semi-infinite space sketched in Fig. 2.2.1 as a basis for deriving the Grahame equation. The Grahame equation describes the relation between the surface charge and the earlier mentioned ζ-potential.

We begin by considering that the charge in the "Gauss pillbox" should vanish:

$$\begin{aligned} 0 &= \int_\Omega (\sigma_e \delta(x) + \rho_e(x)) \mathrm{ds} \\ &= \mathcal{A}\left(\sigma_e + \int_0^\infty \rho_e(x)) \mathrm{d}x\right) \\ \Rightarrow \sigma_e &= \epsilon_r \epsilon_0 \int_0^\infty \frac{\mathrm{d}^2 \varphi(x)}{\mathrm{d}x^2} \mathrm{d}x = -\epsilon_r \epsilon_0 \left.\frac{\mathrm{d}\varphi(x)}{\mathrm{d}x}\right|_{x=0}, \end{aligned} \tag{2.2.40}$$

where Ω is the domain of the Gauss pillbox, ds is the volume integral and $\mathcal{A}$ is the yz area of the pillbox. For the second equality we have used that neither σ_e nor ρ_e depends on the y or the z coordinate. From the second to the third line we have used Eq. (2.2.12) and then integrated the equation.

[9] Be aware that the electric-potential is fixed and that it is zero infinitely far away from the surface.

[10] Note, that $|z_\pm|$ strictly specking equals 1, but the term is kept in the equation to make the result slightly more general.

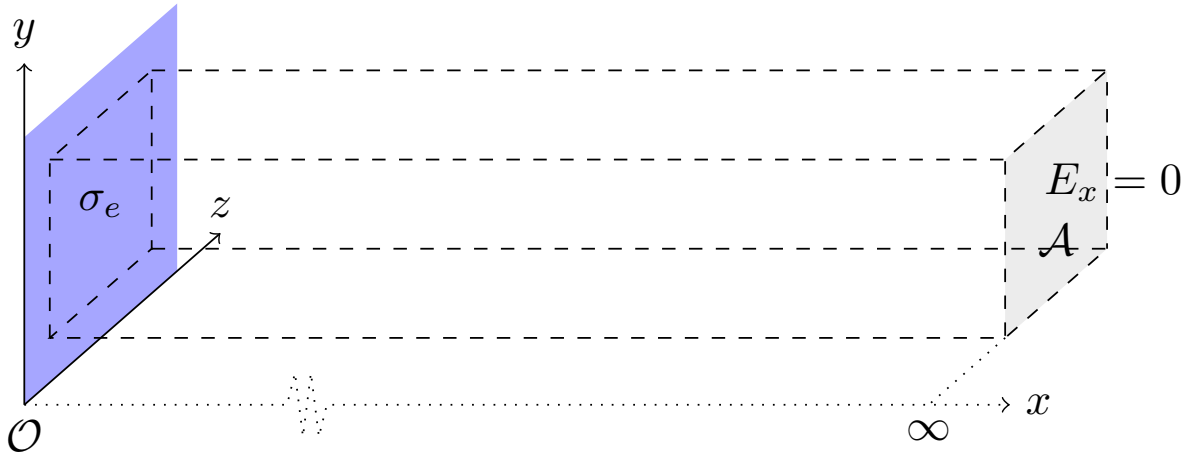

Figure 2.2.1: A semi-infinite geometry, at the plane $x = 0$ we marked a charge wall with surface charge σ_e in blue. The dashed box is a Gauss pillbox the includes the charge wall and goes to infinity, where the electric field is assumed to vanish, the x transverse area of the pillbox is $\mathcal{A}$ as indicated on the figure.

Now to continue we need to find a relation for the electric field's x component. By multiplying the Poisson-Boltzmann equation with $2\frac{\mathrm{d}\varphi}{\mathrm{d}x}$ [11]:

$$2\frac{\mathrm{d}\varphi}{\mathrm{d}x}\frac{\mathrm{d}^2\varphi}{\mathrm{d}x^2} = \frac{\mathrm{d}}{\mathrm{d}x}\left(\frac{\mathrm{d}\varphi}{\mathrm{d}x}\right)^2 = 4\frac{\mathrm{d}\varphi}{\mathrm{d}x}\left[\frac{q_e n^\infty}{\epsilon_r\epsilon_0}\sinh\left(\frac{q_e\varphi}{k_BT}\right)\right], \tag{2.2.41}$$

and then integrating the equation with respect to φ we find:

$$\left(\frac{\mathrm{d}\varphi}{\mathrm{d}x}\right)^2 = \frac{4k_BTn^\infty}{\epsilon_r\epsilon_0}\cosh\left(\frac{q_e\varphi}{k_BT}\right) + c, \tag{2.2.42}$$

Now, in order to ensure consistency with the asymptotic behavior of the electric field in line with what is describe in Fig. 2.2.1 we will have to choose c as:

$$c = -\frac{4k_BTn^\infty}{\epsilon_r\epsilon_0}. \tag{2.2.43}$$

We can now use the half-argument formula for hyperbolic functions to rewrite Eq. (2.2.42) as:

$$\left(\frac{\mathrm{d}\varphi}{\mathrm{d}x}\right)^2 = \frac{2k_BTn^\infty}{\epsilon_r\epsilon_0}\sinh^2\left(\frac{q_e\varphi}{2k_BT}\right). \tag{2.2.44}$$

By taking the square root of Eq. (2.2.44) we get a relation for the x component of the electric field up to a sign, that can be fixed by consistency with Eq. (2.2.20):

$$\left(\frac{\mathrm{d}\varphi}{\mathrm{d}x}\right) = \sqrt{\frac{8k_BTn^\infty}{\epsilon_r\epsilon_0}}\sinh\left(\frac{q_e\varphi}{2k_BT}\right), \tag{2.2.45}$$

[11] Note than the y and z components of the electric field both equals zero due to symmetry.

Finally, introducing Eq. (2.2.45) to Eq. (2.2.40) we arrive at the Grahame equation:

$$\sigma_e = \sqrt{8k_B T n^\infty \epsilon_r \epsilon_0}\sinh\left(\frac{q_e\zeta}{2k_B T}\right) \tag{2.2.46}$$

where ζ is the electric-potential at the surface in equilibrium, sometimes simply called the ζ-potential and is widely used in electro-chemistry.

Note, that the ζ-potential can be somehow generalized to express the voltage difference over the electric doubled layer due to its exponential nature. Also note, that the Grahame equation, like the Poisson-Boltzmann equation, have a linear regime for small values of ζ and that the upper limit for the linearity is around the thermal-voltage where it takes the form [12]:

$$\sigma_e = \sqrt{\frac{2\epsilon_r\epsilon_o n^\infty}{k_B T}}\zeta = \frac{\epsilon_r\epsilon_0\zeta}{\lambda_D} \tag{2.2.47}$$

Streaming Potential and the Electro-viscous Effect

The concept a streaming-potential is an out-of-equilibrium phenomenon and is typically addressed theoretical in steady state. Consequently, we now depart from equilibrium, however our insight in the equilibrium case will still be of great value when treating this topic as the result still have some validity under certain symmetries and since we are not to far away form equilibrium.

The derivation of the streaming-potential and the related electro-viscous effect will be carried out in an infinity long tube, in the linear-regime (Debye-Hückel approximation) of the Poisson-Boltzmann equation where it takes the simpler form [44, 63]

$$\nabla^2\varphi = \frac{1}{\lambda_D^2}\varphi, \tag{2.2.48}$$

one sees that the Debye length λ_D sets the characteristic decay-length the of solution in the semi-infinite case given in Fig. 2.2.1.

As we consider an infinite long channel we will assume translation invariance along both the flow-direction and in the non-bounded transverse-direction. Solving the linearized Poisson-Boltzmann equation under the boundary conditions that the electric-potential at the channel walls equals the ζ-potential ($\varphi\big|_{x=\pm a} = \zeta$) and that its transverse derivative is zero in the center of the channel, ($\frac{\mathrm{d}}{\mathrm{d}x}\varphi\big|_{x=0} = 0$), yields:

$$\varphi(x) = \zeta\frac{\cosh(\kappa x)}{\cosh(\kappa a)}, \tag{2.2.49}$$

where κ is the inverse Debye length λ_D. Note that the definition of ζ-potential is a bit murky if the radius a does not go to infinity.

From the electric potential, Eq. (2.2.49), we get the charge density via inspection of Eq. (2.2.48) in conjunction with Eq. (2.2.12) to be:

$$\rho_e(x) = -\frac{\zeta\epsilon_r\epsilon_0}{\lambda_D^2}\frac{\cosh(\kappa x)}{\cosh(\kappa a)}. \tag{2.2.50}$$

[12] The thermal-voltage for a monovalent solution is around $25\ \mathrm{mV}$ at room temperature corresponding to a surface charge of $0.19\ \mathrm{mC/m^2}$ for an ion concentration at $0.01\ \mathrm{mol/m^3}$.

Up until this point our solution have been exact under the approximation. However, we want to introduce a streaming-electric-field E_z in the axial direction in order to model a no charge-flux thorough the channel.

An electric field along the axial direction is a bit problematic in terms of the electric potential, as it must divergence, but if E_z is independent of z we still have translation invariance and the result in Eqs. (2.2.49) and (2.2.50) should still be valid. For E_z we will furthermore assume that it is independent of the tube's radial and angular coordinates as well.

Now, considering the Stokes equation 2.2.13 forced by the electro static force from E_z acting on the free charge, along a constant pressure gradient in the z-direction, $\frac{\mathrm{d}}{\mathrm{d}z}P$. Noting, that the velocity field only can have a non-trivial dependence on x due to symmetry leads to a balance between the pressure gradient in the x-direction, $\frac{\mathrm{d}}{\mathrm{d}x}P$, and the x-component of electric forces due to the electric-double-layer. The equation for the velocity field hence becomes:

$$\mu\frac{\partial^2 u_z}{\partial x^2} = -\frac{\partial P}{\partial z} - \rho_e E_z. \tag{2.2.51}$$

Now, inserting the charge density form the Possion-Boltzmann equation, Eq. (2.2.50) into Eq. (2.2.51) and solving it under the no-slip boundary on the tube walls leads to:

$$u_z(x) = \frac{\frac{\partial P}{\partial z}}{2\mu}\left(a^2 - x^2\right) - \frac{\epsilon_r\epsilon_0\zeta E_z}{\mu}\left(1 - \frac{\cosh(\kappa x)}{\cosh(\kappa a)}\right). \tag{2.2.52}$$

In order to continue we now need to find E_z by using the non-charge-flux assumption. Consider the axial component of charge-current-density giving by Eqs. (2.2.2), (2.2.6) and (2.2.9). Obviously, the diffusion term vanishes per translation invariance, so we are left with the following:

$$J_{e(z)} = \rho_e(x)u_z(x) + \frac{2Dq_e^2}{k_BT}E_z n^\infty \cosh\left(\frac{q_e\varphi(x)}{k_BT}\right), \tag{2.2.53}$$

Note that $\cosh$ in the second term is due to the fact that it is the sum of number-densities weighted with their valency squared. Since the second term can only vanish for a vanishing electric field and the first term does not vanish for a Poiseuille flow, the two terms need to be at balance. In order to find the electric field that balance the two terms fluxes we integrate them over the cross section.

Starting by integrating the velocity term in Eq. (2.2.53) to get the flux, note that due to symmetry the y-integration is trivial and just gives the with $\mathcal{L}$:

$$\mathcal{L}\int_{-a}^{a}\rho_e(x)u_z(x)\mathrm{d}x = -2\mathcal{L}\int_0^a\left[\frac{\frac{\partial P}{\partial z}}{2\mu}\left(a^2-x^2\right) - \frac{\epsilon_r\epsilon_0\zeta E_z}{\mu}\left(1-\frac{\cosh(\kappa x)}{\cosh(\kappa a)}\right)\right]\frac{\zeta\epsilon_r\epsilon_0}{\lambda_D^2}\frac{\cosh(\kappa x)}{\cosh(\kappa a)}\mathrm{d}x \tag{2.2.54}$$

$$\begin{aligned}
&= -\frac{a^2\mathcal{L}\frac{\partial P}{\partial z}\zeta\epsilon_r\epsilon_0}{\mu\lambda_D^2}\int_0^a\frac{\cosh(\kappa x)}{\cosh(\kappa a)} - \frac{x^2}{a^2}\frac{\cosh(\kappa x)}{\cosh(\kappa a)}\mathrm{d}x \\
&\quad + \frac{2\mathcal{L}\epsilon_r^2\epsilon_0^2\zeta^2 E_z}{\mu\lambda_D^2}\int_0^a\frac{\cosh(\kappa x)}{\cosh(\kappa a)} - \frac{\cosh^2(\kappa x)}{\cosh^2(\kappa a)}\mathrm{d}x \\
&= -2\mathcal{L}a\frac{\partial P}{\partial z}\Omega\left[1 - \frac{\lambda_D}{a}\tanh(\kappa a)\right] \\
&\quad + \frac{\mathcal{L}a\Omega^2 E_z\mu}{\lambda_D^2}\left[\frac{\lambda_D}{a}\tanh(\kappa a) - \operatorname{sech}^2(\kappa a)\right],
\end{aligned}$$

where $\Omega = \frac{\epsilon_r \epsilon_0 \zeta}{\mu}$. Integrating the second term of the charge current, Eq. (2.2.53), is apparently not possible on a closed form as the electric-potential have a rather non-trivial form [13]

$$\begin{aligned} \frac{2\mathcal{L}Dq_e^2 n^\infty}{k_B T} E_z \int_{-a}^{a} \cosh\left(\frac{q_e \zeta}{k_B T} \frac{\cosh(\kappa x)}{\cosh(\kappa a)}\right) \mathrm{d}x \\ = \frac{2\mathcal{L}aDq_e^2 n^\infty}{k_B T} E_z \int_0^1 2\cosh\left(\frac{q_e \zeta}{k_B T} \frac{\cosh(\kappa a X)}{\cosh(\kappa a)}\right) \mathrm{d}X, \end{aligned} \tag{2.2.55}$$

where $X = x/a$. If multiplied with n^∞ the integral in the last line is half the total amount of charge carries in the channels cross section. It has a minimum value when $\zeta = 0$ or if $\lambda_D \gg a$ where it equals unity so one recovers the bulk conductivity. Its maximum is obtained when $\lambda_D \ll a$ and here it simply becomes $2\cosh[(q_e\zeta)/(k_B T)]a$. Below we will abbreviate this integral F_{cc}. Now we can get an expression for E_z under the already advertised assumption that the charge flux vanish:

$$\left.\frac{E_z}{\frac{\partial P}{\partial z}}\right|_{J_{e(z)}=0} = \frac{\epsilon_r \epsilon_0 \zeta k_B T}{\mu D q_e^2 n^\infty F_{cc}} f(\kappa a, \beta). \tag{2.2.56}$$

Where the last term $f(\kappa a, \beta)$ is:

$$f(\kappa a, \beta) = \frac{1 - \frac{\lambda_D}{a}\tanh(\kappa a)}{1 + \frac{\beta}{F_{cc}}\left(\frac{\lambda_D}{a}\tanh(\kappa a) - \mathrm{sech}^2(\kappa a)\right)}, \tag{2.2.57}$$

and where β is:

$$\beta = \frac{\Omega^2 \mu k_B T}{2\lambda_D^2 D q_e^2 n^\infty} = \frac{\epsilon_r \epsilon_0 \zeta^2}{\mu D}. \tag{2.2.58}$$

If we identify $\frac{2Dq_e^2 n^\infty}{k_B T}$ in Eq. (2.2.56) as the conductivity, we get the Helmholtz-Smoluchowski equation [82] with some correction factors that deal with the finite extent of the Debby layer, F_{cc}, and a geometrical factor, $f(\frac{a}{\lambda_D}, \beta)$ [14]. From the Helmholtz-Smoluchowski equation (or Eq. (2.2.56)) one can also define the so called streaming potential by isolating the electric field and integrating over the length of the channel:

$$V_{str} = -\frac{\epsilon_r \epsilon_0 \zeta k_B T}{\mu D q_e^2 n^\infty F_{cc}} f(\kappa a, \beta) \Delta P, \tag{2.2.59}$$

where V_{str} is the stream potential i.e. the potential-difference between two points at the ends of a infinite tube with and ΔP is likewise the pressure-difference between the same two points. Note, that in reality the relation is used for finite length objects where one would simply use the drops in voltage and in pressure over the channels length and assume that entry effects are minor.

To continue the endeavor to find an expression for the electro-viscous effect we use the newly found relation between the streaming-electric-field and the applied pressure gradient Eq. (2.2.56) to eliminate the streaming-electric-field in the equation for the axial velocity field Eq. (2.2.52) and thus finding an equation that only depends on the axial component of the pressure gradient:

$$u_z(r) = \frac{\frac{\partial P}{\partial z}}{2\mu}\left[\left(a^2 - x^2\right) - \frac{4\beta\lambda_D^2}{F_{cc}} f(\kappa a, \beta)\left(1 - \frac{\cosh(\kappa x)}{\cosh(\kappa a)}\right)\right]. \tag{2.2.60}$$

[13] It could be expressed as an infinitive sum of generalized hypergeometric functions, but that is hardly more convenient.

[14] The Helmholtz-Smoluchowski limit of Eq. (2.2.56) is more precisely obtained in the limit where $\frac{a}{\lambda} \gg 1$ as both F_{cc} and $f(\frac{a}{\lambda_D}, \beta)$ goes towaqrds 1 in this limit.

Now, integrating the velocity over the cross section will yield the mass-flux of the fluid:

$$Q_z = \frac{2\mathcal{L}a\frac{\partial P}{\partial z}}{3\mu}\left[a^2 - \frac{6\beta\lambda_D^2}{F_{cc}} f\left(\kappa a, \beta\right)\left(1 - \frac{1}{\kappa a}\tanh(\kappa a)\right)\right], \tag{2.2.61}$$

where Q_z is the mass-flux. A more efficient way of handling the electric braking can be obtained by introducing the electric-viscosity μ_e so equation Eq. (2.2.61) becomes:

$$Q_z = \frac{2\mathcal{L}a^3\frac{\partial P}{\partial z}}{3\mu_e}, \tag{2.2.62}$$

and the electric viscosity must then be give as:

$$\mu_e = \mu\left[1 - \frac{6\beta}{\kappa^2 a^2 F_{cc}} f\left(\kappa a, \beta\right)\left(1 - \frac{1}{\kappa a}\tanh(\kappa a)\right)\right]^{-1}, \tag{2.2.63}$$

This result concludes the mathematical treatment of the streaming potential and the electro-viscous effect, however we will note that we have plotted μ_e for relevant parameters in Fig. 2.2.2. Now we

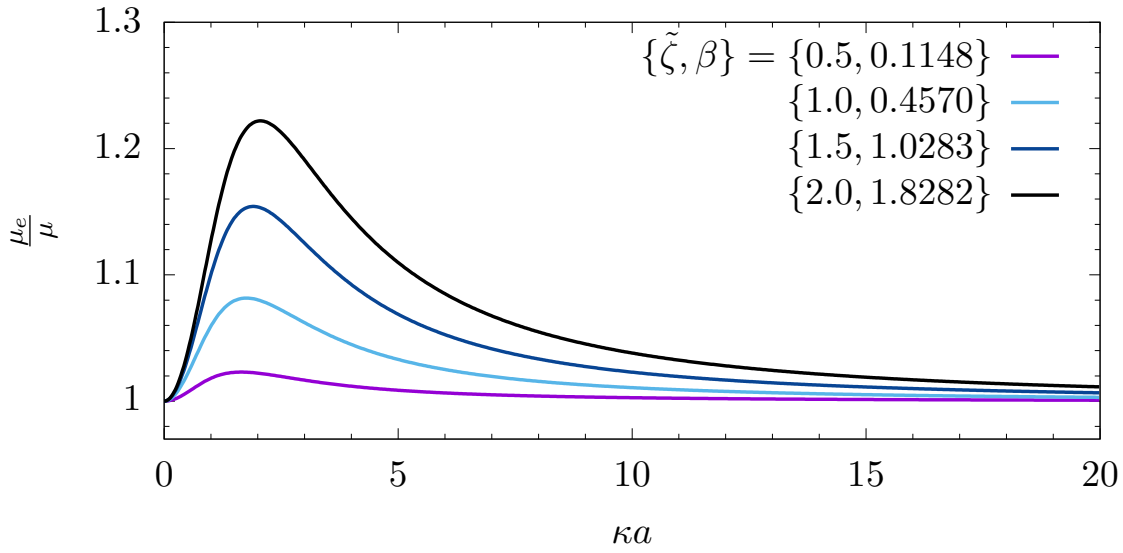

Figure 2.2.2: Here we have plotted electro viscosity, μ_e for different values of ζ and related β values. We see that the electro-viscosity mush more relevant the higher the surface potential and that it peaks when the channel width is 4 times the Debye length.

will turn to discussing the phenomenological origin of the streaming potential in finite channels.

Phenomenology of the Streaming-potential in Finite Tubes.

With a basic understanding of the effects due to the streaming potential in infinite tubes we will now turn to discuss its phenomenological origin in the finite counterpart.

In our derivation of equation Eq. (2.2.59) the streaming potential was mainly introduced in order to have a zero flux condition on the charge-current in the case of steady state. However this hardly gives an explanation of the physical mechanism behind the streaming-potential in realistic systems. So let us consider a finite tube with an inlet and outlet as showed on Fig. 2.2.3.

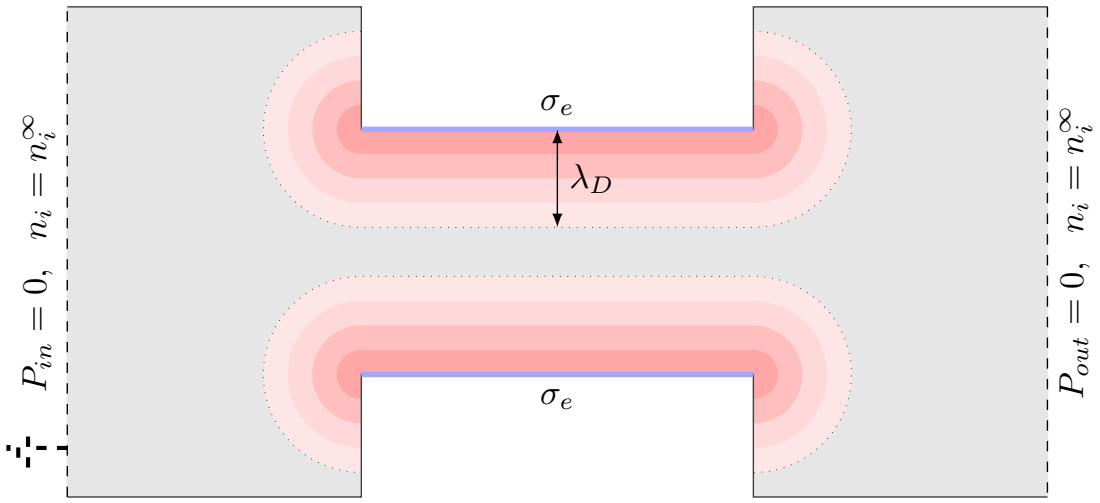

Figure 2.2.3: A micropore with homogeneous surface charge σ_e in equilibrium, the Debye length λ_D is set by the inlet and outlet ion-number-density n_i^∞, and screens the surface charge completely on scales much larger than the Debye length. The red shade in the channel is to indicate the electric double layer.

In equilibrium, and for that matter to some extend also in steady state, the electric double layers are locally screening all long-range electric effects. However, in the channels things differ quite dramatical, e.g. in the case of equilibrium the advection charge current is zero by definition[15], which implies that there can be no conduction-charge-current in excess of what balance the diffusion-charge-current at the interfase.

In steady-state, as we do not have that the currents vanish locally but only can assume them to be time independent along all other quantities, the time independence of the currents implies that all cross-sectional-fluxes of a certain quantity must be equal since the channel walls does not allow any flux to pass. Now considering the boundary condition that the inlet and outlet enforces on the value of cross-sectional-fluxes. The fluid-mass-flux is specified implicitly through the pressure, geometrical and electro-viscous effects, likewise to the specification of the ion-number-flux by the inlet velocity. The charge-current-flux is vanishing if the electric-fields at the inlet and outlet are specified to be zero and the charge density is zero at the inlet and outlet.

Knowing that the cross-sectional-charge-flux should vanish throughout the channel and that we will have advective transport of charges in the double layers we must conclude that there must be either a conduction or a diffusion-charge-current to counter for it. Diffusive-charge-currents does not exist without a departure from electro-neutrality meaning that they are only found near charged interfaces as when they are present they will lead to conduction-charge-currents [16]. Conduction-charge-currents on the other hand can account for huge amounts of electric transport even in the case of charge neutrality, but it needs a electric-field to drive it. The origin of such a electric-field stems from a distortion of the double layers at the inlet and outlet due to the imposed flow efficiently generating an electric ”dipole”; for an illustration see Fig. 2.2.4 [44].

Now, with a good phenomenological and theoretical insight in electrohydrodynamics in confide spaces we would like to turn to the numerical methods we have used to solve the full system of equations given in Section 2.2.1 in three dimensions. The following section is dedicated to this subject.

[15]We understand equilibrium as all currents i.d.: $\mathbf{J}_i$,$\mathbf{J}_e$ and $\mathbf{u}$ have to be zero locally.

[16]This in principal is what can be seen in the electric double layer under strict equilibrium conditions.

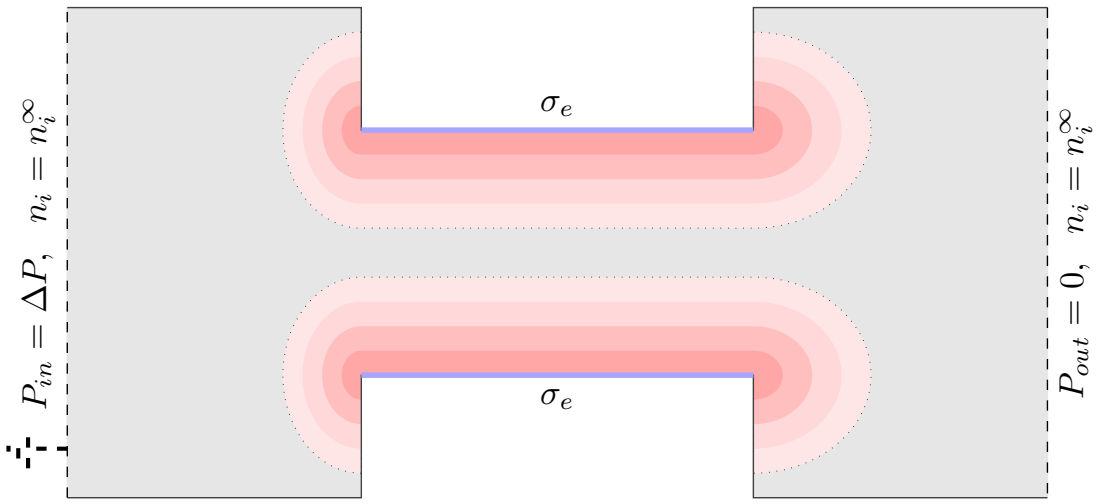

(a)

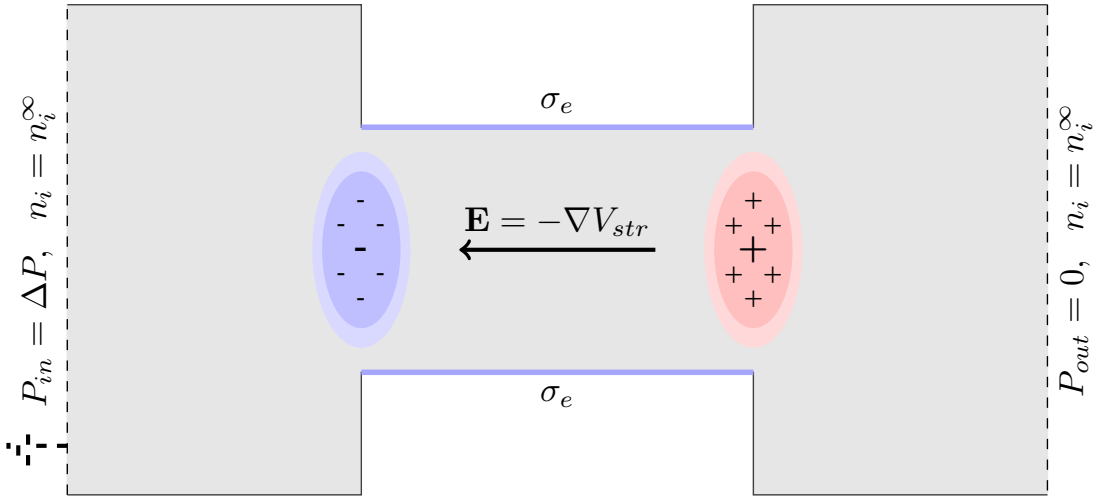

(b)

Figure 2.2.4: (a) The same microchannel as in Fig. 2.2.3 but with at pressure difference ΔP that drives the flow from left to right. The flow leads to a distortion of the electric double layer as illustrated by the distortion of the red shade which in turn generate a streaming potential in its steady-state configuration. (b) An illustration of the difference between equilibrium and steady-state electric double layer. One gets an electric-dipole in the channel that breaks the flow as it acts on the electric double layer. Note that the surface charge in this figure in assumed to be negative.

2.3 Numerical Setup

Numerical studies of coupled systems consisting of the Nernst-Planck equation, the Poisson and the time dependent Stokes equation, sometimes called the Poisson-Nernst-Planck-Stokes Problem(PNPS-Problem) have been investigated broadly in one and two dimensional cases.

COMSOL[17] [44, 18, 35], however also a lattice Boltzmann approach have been used in the studies of transients [87].

Three dimensional simulations have however not been investigated much as this increase in the computational demands is quite significant. Some investigations have, however, been done in FEniCS[18] for biological membranes [48].

So what we have done in our study is to implant our own three dimensional FEniCS solver for the steady state PNPS-problem. Before going in to details of the implantation let us give a short introduction to Finite element methods.

2.3.1 The Finite Element Method

The finite element method (FEM) is one of the most used computational methods. It is especially usefull in situations where the geometry is complicated as it uses locally defined basis functions as opposed to the otherwise similar spectral methods' globally defined functions. Furthermore, the simplicity of formulating finite element methods for all kinds of partial differential equations makes it a flexible and versatile tool.

The increased geometrical flexibility of the finite element method comes with increased computational costs and with worse converges rates compared to spectral methods in simple geometrics.

It should be mentioned that also the so-called lattice Boltzmann method is an efficient method for flow in complex geometries, especially for transient problems such as turbulent flow. As we are mainly interested in steady state results such kinetic based approaches are however of little use.

We will in the coming section describe the basic steps in driving a finite element method for partial differential equations.

The Galerkin Method

The Galerkin method is a way to convert a linear partial differential equation into a set of linear algebraic equations. The introduction given here is not aimed to be precise in a mathematical sence but is mainly intended to give an introduction to the origins of the Galerkin method.

If one whats to use the Galerkin method on non-linear equations one has to provide some kind of linearizion first, one can for instance utilize the Newton method. We will cover the Newton method explicitly below as it is needed for the coupled Poisson-Nernst-Planck equation.

For the derivation of the Galerkin method let us start by considering a linear partial differential equation given on some domain Ω with a surface Γ of the form:

$$\mathcal{D}u = f, \tag{2.3.1}$$

[17] COMSOL is a commercial available finite element solver with a rather extensive implementation of physical equations both for time dependent and steady state simulations.

[18] FEniCS is a free high performance finite element API allowing one to implement general problems with relatively ease. At broader introduction is given in section Section 2.3.2.

where u is a solution of the equation in the domain Ω that is satisfying the boundary conditions given on Γ [19], f is some well-behaved function and $\mathcal{D}$ is a linear differential operator on the form:

$$\mathcal{D} = k_1\nabla^2 + \nabla \cdot \mathbf{k} + k_2, \tag{2.3.2}$$

where the $\mathbf{k}$ is a space dependent vector, k_1 is some positive constant and k_2 is a constant [20].

Now let us define a scalar product between the solutions u and some the so called test functions ω that have the property that they equals zero on the boundary Γ as follows[21]:

$$\langle \omega, u \rangle = \int_\Omega \omega u \, \mathbf{d}v. \tag{2.3.3}$$

This makes it possible to test our differential equation from Eq. (2.3.1) with ω to get the following equation:

$$\int_\Omega \omega \left[\mathcal{D}u - f\right] \, \mathbf{d}v = 0, \tag{2.3.4}$$

Now, by using linearity of the differential operator and the Stokes theorem we can get what is effectively a higher dimensional partial derivative to reform Eq. (2.3.4):

$$\int_\Gamma \omega \left[k_1\nabla u + \mathbf{k}u\right] \cdot \mathbf{n} \, \mathbf{d}s - \int_\Omega \nabla\omega \cdot \left[k_1\nabla u + \mathbf{k}u\right] - k_2\omega u + \omega f \, \mathbf{d}v = 0, \tag{2.3.5}$$

where we have used the form of $\mathcal{D}$ given in Eq. (2.3.2).

Using the definition of the inner product from Eq. (2.3.3) allows us to rewrite the equation as:

$$\begin{aligned} A(\omega, u) + b(\omega) &= 0, \\ A(\omega, u) &= \langle \nabla\omega, \left[k_1\nabla u + \mathbf{k}u\right] \rangle - \langle k_2\omega, u \rangle \, , \\ b(\omega) &= \langle \omega, f \rangle + \langle \omega, B_{NR} \rangle_\Gamma \, , \end{aligned} \tag{2.3.6}$$

Here $A(\omega, u)$ is a bilinear map and $b(\omega)$ is a linear map as the term $\left[k_1\nabla u + \mathbf{k}u\right] \cdot \mathbf{n}$ is replaced with the Nuemann/Robin boundary conditions denoted by B_{NR}.

The form in Eq. (2.3.5) or Eq. (2.3.6) is know as the weak form of Eq. (2.3.1) as a solution to Eq. (2.3.1) always satisfy Eq. (2.3.5) but not the other way around. It should also be noted that Eq. (2.3.5) allows us to relax the differentiability condition on u so that is only one time differentiable instead of two times differentiable. That Eq. (2.3.6) yields weak solutions is sometimes known as the Galerkin principle as well.

In order to progress from the Galerkin principle to something that can be implemented on a computer we will need to expand the solution u and the test function ω on some linear independent finite basis. We denote these finite basis's functions ϕ_i, where i is the numbering, and write out the approximation of solution u and test function ω in the basis [22]:

$$u_d = u_\Gamma(\mathbf{x}) + \sum_{i=1}^{N} u_i\phi_i(\mathbf{x}) \tag{2.3.7}$$

$$\omega_d = \sum_{i=1}^{N} \omega_i\phi_i(\mathbf{x}) \tag{2.3.8}$$

[19] u is throughout the derivation dealt with as a scalar but there is no problems in extending it be a tensor of an arbitrary rank (the vector being obviously the first extension), only it will have to carry some extra indies.

[20] Note that the form of $\mathcal{D}$ is not choosen particular general, but it covers all the cases we will consider in practice.

[21] Note that u and ω are not found in the same space as u have to satisfy some boundary conditions.

[22] ϕ_i can in principal be any sufficiently well-behaved function that goes to zero on Γ, in our case being at least one time differential and having a H^1 norm would be adequate.

where u_d or ω_d is the approximated solution resp. test function of our equation in the finite basis, $u_\Gamma(\mathbf{x})$ is a function that satisfy the Dirichlet boundary conditions, N is the number of basic functions and u_i or ω_i is coefficients like the ones in a Fourier sum.

In addition we can define derivatives of u_d and ω_d in a similar manner:

$$\nabla u_d = \nabla u_\Gamma(\mathbf{x}) + \sum_{i=1}^{N} u_i \nabla \phi_i(\mathbf{x}) \tag{2.3.9}$$

$$\nabla \omega_d = \sum_{i=1}^{N} \omega_i \nabla \phi_i(\mathbf{x}) \tag{2.3.10}$$

This gives us all we need to reformulate Eq. (2.3.5), along some Einstein notation for the sums. In the finite basis we can write Eq. (2.3.5) as:

$$\begin{aligned} -\int_\Omega \omega_i \nabla \phi_i(\mathbf{x}) \cdot [k_1 u_j \nabla \phi_j(\mathbf{x}) + \mathbf{k}(\mathbf{x}) u_j(\mathbf{x}) \phi_j(\mathbf{x})(\mathbf{x})] - k_2 \omega_i \phi_i u_j \phi_j + \omega_i \phi_i(\mathbf{x}) f(\mathbf{x})\, \mathbf{d}v \\ -\int_\Omega \omega_i \nabla \phi_i(\mathbf{x}) \cdot [k_1 \nabla u_\Gamma(\mathbf{x}) + \mathbf{k}(\mathbf{x}) u_\Gamma(\mathbf{x})] - k_2 \omega_i \phi_i(\mathbf{x}) u_\Gamma(\mathbf{x}) + \omega_i \phi_i(\mathbf{x}) f(\mathbf{x})\, \mathbf{d}v \\ + \int_\Gamma \omega_i \phi_i(\mathbf{x}) B_{NR}(\mathbf{x})\, \mathbf{d}s = 0, \end{aligned} \tag{2.3.11}$$

where we have explicitly stated that $\mathbf{k}$ and $\mathbf{f}$ can depend on space.

Now, by noting that the coefficients v_i and w_i is independent of space we can rewrite Eq. (2.3.11) as:

$$\begin{aligned} -\omega_i \int_\Omega \nabla \phi_i(\mathbf{x}) \cdot [k_1 \nabla \phi_j(\mathbf{x}) + \mathbf{k}(\mathbf{x}) \phi_j(\mathbf{x})] - k_2 \phi_i(\mathbf{x}) \phi_j(\mathbf{x})\, \mathbf{d}v u_j \\ -\omega_i \int_\Omega \nabla \phi_i(\mathbf{x}) \cdot [k_1 \nabla u_\Gamma(\mathbf{x}) + \mathbf{k}(\mathbf{x}) u_\Gamma(\mathbf{x})] - k_2 \phi_i(\mathbf{x}) u_\Gamma(\mathbf{x})\, \mathbf{d}v \\ + \omega_i \int_\Omega \phi_i(\mathbf{x}) f(\mathbf{x})\, \mathbf{d}v + \omega_i \int_\Gamma \phi_i(\mathbf{x}) \mathbf{g}(\mathbf{x}) \cdot \mathbf{n}\, \mathbf{d}s = 0, \end{aligned} \tag{2.3.12}$$

Now, by defining the following matrix A_{ji} and vector b_i:

$$A_{ji} = -\int_\Omega \nabla \phi_i(\mathbf{x}) \cdot [k_1 \nabla \phi_j(\mathbf{x}) + \mathbf{k}(\mathbf{x}) \phi_j(\mathbf{x})] - k_2 \phi_i(\mathbf{x}) \phi_j(\mathbf{x})\, \mathbf{d}v \tag{2.3.13}$$

$$\begin{aligned} b_i = \int_\Omega \nabla \phi_i(\mathbf{x}) \cdot [k_1 \nabla u_\Gamma(\mathbf{x}) + \mathbf{k}(\mathbf{x}) u_\Gamma(\mathbf{x})] - k_2 \phi_i(\mathbf{x}) u_\Gamma(\mathbf{x})\, \mathbf{d}v \\ + \int_\Gamma \phi_i(\mathbf{x}) \mathbf{g}(\mathbf{x}) \cdot \mathbf{n}\, \mathbf{d}s + \int_\Omega \phi_j(\mathbf{x}) f(\mathbf{x})\, \mathbf{d}v = 0, \end{aligned} \tag{2.3.14}$$

we get the following algebraic equation:

$$\omega_i A_{ij} u_j + \omega_i b_i = 0, \tag{2.3.15}$$

As this, however, should hold for all ω_d it is equivalent the linear equation:

$$A_{ij} u_j + b_i = 0, \tag{2.3.16}$$

Using this equation to finding u_j is known as the Garelkin method.

Now in oder to use this equation in any practical circumstances we need to calculate A_{ij}, and for that matter b_i. This of course can be done in any linear independent basis functions ϕ one would like to choose but then the matrix would in general be dense [23]. A simple way to avoid a dense matrix is to choose the ϕ_i to be mutual orthogonal on their domain Ω [24]. Another more general applicable way is to choose basis functions with compact support in such a way that they only overlap their neighboring functions.

To make this clearer let us discretize the domain Ω. This can be done many ways, but a common way to do it is to approximate the surface with a polyhedron in three dimension or with polygon in two dimension, and then subdivide it into small and simple polyhedrons/polygons like tetrahedrons/triangles. We will consider tetrahedrons and we note that for the union of them the following should hold:

$$\Omega = \bigcup_{t=1}^{M} \Omega^t, \tag{2.3.17}$$

where Ω^t is the domain of the t'ed tetrahedron and M is the number for tetrahedrons used to form Ω [25].

Now we label each vertex of the tetrahedrons by an i. Note, that each vertex will be shared by several tetrahedrons and that we do not allow for the vertex of a tetrahedron to be on the facet of one of the other tetrahedrons. The total number of vertices is called N.

In this model we can associate every vertex with a piecewise linear function that is zero on all other verities but between itself and its neighboring sits where it is an interpolation between zero and some finite value given by u_i [26].

Such a choice of basis functions Eq. (2.3.16) is known as the finite element Galerkin method and Dirichlet boundary conditions can be fixed by setting the value of u_i equal to u_Γ on the boundary and then just solving the homogeneous problem with the appropriate Neumann conditions, hence the integral containing u_Γ disappears from b_i.

Finally in order to solve the equation Eq. (2.3.16) one simply have to invert A_{ij} and multiply it on b_i which yields:

$$v_i = A^{-1}_{ij} b_i, \tag{2.3.18}$$

However, the inversion of a matrix scales computational rather much (i.e. bad) with size so in a three dimensional problem one will have to turn to less memory intensive methods such as Krylov subspace iterative solvers. This we will cover in the next section.

Krylov Subspace Iterative Solvers

Will here introduce briefly the idea of krylov subspace iterative solvers but refer to more specialized literature for more precise and extensive treatment of the subject[65]. Krylov subspace solvers utilizes

[23] A dense matrix has in general no non-zero components and is consequently from a computational point of view unmanageable even for moderate large amounts of basis functions.

[24] Choosing orthogonal basis functions is precisely what is done in the so-called spectral methods. But such basis functions with the right completeness qualities are only known in highly symmetric cases.

[25] Note, that in order to simplify the notation we do not distinguish between the possible smooth domain Ω and it's polyhedron counterpart.

[26] One can use more elaborate higher polynomial elements to get a better local approximation of the solution but one would then have to fix more constants. For an overview of the more elaborate higher polynomial elements see `https://femtable.org/`.

a so called Krylov sequence to from at a basis from a initial residual iteratively, by some matrix-vector operation. After each iteration the found basis is used to minimize residual and if the residual is smaller that some tolerance, one assume the method have converges to a good approximation of the solution and stops further iteration. One can use different Krylov solvers to generate a basis, but typical the choice depends problem that need to be solved. Further to get better converges and robustness one can apply what is known preconditioners to the problems, which typical some transformation of the problem or the use of partial solution that makes the Krylov solver reliable. Both the Krylov solvers and preconditions we have used will be mentioned in context with the equation they are meant to solve. From this brief note on Krylov solvers let us introduce the framework where we have implemented our solves FEniCS.

2.3.2 FEniCS

As finite element methods are rather common apporaches for solving partial differential equations, there already exist extensive computational liberates for the core-components of the method and furthermore these components can be found in assemblies under general finite element platforms.

One such platform is known as FEniCS [3]. The FEniCS platform consists of different comments that makes setting up and solving finite element problems straight forward for simple linear equations and for more complicated none-linear equations still quite seamless. The main components of FEniCS are: DOLFIN [42, 40], FFC [27, 41], UFL [2, 6], FIAT [25, 26] and UFC [5, 4].

DOLFIN is the API component and exists for both PYTHON and in C++ and it is what is used to write scricps that sets up a problem, solves it, store data, etc. The commands given in DOLFIN are passed on to the other components of FEniCS which compiles the commands down to high preforming C++ that can be parallelized to use efficiently in the order of 10^4 parallel processors.

One of the big advantages of FEniCS from a physicists point of view is that it only needs a weak form of the equation in question along the appropriate boundary condition in order to implement a solver, the rest of the Galerkin procedure is done by the computational back end.

2.3.3 Numerical Schemes

As the steady state Poisson-Nernst-Planck-Stokes problem is highly non-linear one can not just simply solve the problem using the finite element method directly, one have to find some way of linearizing the system of equations.

The standard way of doing this is to apply some sort of Newton method, hence linearizing the full equation system around some initial guess and then iterate until it converges. The Newton method is however not guaranteed to converge of any initial guess and furthermore it is very memory intensive to run for a problem with several different fields.

Another approach would be to solve the equations decoupled in sequence and then iterate this procedure until it converges. Such decoupled methods typical have the advantage that the sub-problems are linear in nature and consequently can be solve by quite easily. The down side shows off when the coupling term is too strong so that the rate of convergence can be very long.

In the specific case of the steady state Poisson-Nernst-Planck-Stokes problem one will turn to a so-called hybrid method [48] as the Poisson and Nernst-Planck equations are strongly coupled and the Stokes equation only are weakly coupled to the two other equations. The hybrid method in this context means that one solves the Poisson and Nernst-Planck equations coupled with a Newton method and then solves the Stokes equation as a normal linear equation with an electric force term. This procedure is then repeated until convergence.

Note, that in order to increase chance of convergence of the Poisson-Nernst-Planck problem we will provide an initial guess on the solution using a solution of the linearized Poisson-Boltzmann equation. A flow chart of the hybrid method can be found in figure Algorithm 1.

Algorithm 1 Hybrid Solver for Stokes–Poisson–Nernst–Planck system (from [48]).

1: Solve Stokes equation Eqs. (2.3.23) and (2.3.24) to obtain $(\vec{u}, P)$.
2: Solve the linearized Poisson–Boltzmann equation (2.3.28) to get an initial guess for (ϕ, n_+, n_-).
3: Solve one Newton step Eq. (2.3.37) in Poisson–Nernst–Planck problem Eqs. (2.2.27) and (2.2.30) for $(\delta\phi, \delta n_+, \delta n_-)$.
4: Update $(\phi, n_+, n_-) \leftarrow (\phi + \delta\phi, n_+\delta n_+, n_- + \delta n_-)$.
5: Store $(\vec{u}_{old}, P_{old}) \leftarrow (\vec{u}, P)$
6: Solve Stokes equation to get $\vec{u}$ and P.
7: Find $(\delta\vec{u}, \delta P) \leftarrow (\vec{u}_{old} - \vec{u}, P_{old} - P)$
8: Compute Error $:= \frac{1}{2}\left(\frac{\|(\delta\phi,\delta n_+,\delta n_-)\|}{\|(\phi,n_+,n_-)\|} + \frac{\|(\delta\vec{u},\delta P)\|}{\|(\vec{u},P)\|}\right)$
9: If Error $< \tau$, stop.
10: Else, go to Step 3 for another iteration.

With this general idea of the numerical scheme let us turn to discuss the specific sub-problems. Let us start with the Stokes equation, then the linearized Poisson-Boltzmann equation and endwith the Nernst-Planck-Poisson problem.

Weak Form of the Stokes Equation

The Stokes equation is quite well known in the context of the finite element method and standard methods exits to solve the equation. However, in the context of incompressible flow things become a bit more complicated due to the saddle point structure of the equation. The challenges of the instabilities of the Stokes problem can in be handled by satisfying the Bobuska-Brezzi condition [33] leading to the use of so called Taylor-Hood elements or other more advanced types of elements. This however only solves the problem of instability of the solution and not how to actual solve the problem itself.

Off course, if one would use a direct inversion algorithm like the Upper-Lower-decomposition to solve the system there is no theoretical troubles as the Stokes equation is linear. But there is a computational problem as all known direct inversion algorithm scales rather bad both concerning memory use and regarding the floating point operation needed . This means that epically in 3 dimensional simulations one would like to utilize Krylov subspace solves. Here it turns out that the Stokes problem, again due to its saddle point structure, is particular badly preconditioned and will typical not converge sufficiently fast to be usefull[27].

Luckily there exist so-called triangular preconditions for the Stokes problem that rely on a Schur complement to precondition the equation in a better way which should make it possible for a Kylov solver to solve the resulting equation in three iterations when using the exact Schur complement[17]. There is however a slight problem concerning the Schur complement in relations to the Stokes problem: It turns out to result in a dense matrix, which is not really fit for computations.

But everything is not totally lost as one can approximate the Schur complement in different ways. One such way is known as the pressure-convection-diffussion preconditioner, or PCD preconditioner for short. Which we have used for solving the Stokes problem [17, 59]. We will not go in to further de-

[27] Actual from my own experiences it does not converge at all.

tails on the PCD preconditioner as it i as big topic itself, and we have utilized an already implemented version called FENaPack [28].

With this introduction to the preconditioner let us recapitulate the dimensionless steady state Stokes equation as found in Section 2.2.3[29]:

$$-\nabla P + \nabla^2 \mathbf{u} = -\frac{R^2}{2\lambda_D^2}\rho_e \nabla\varphi, \tag{2.3.19}$$

$$\nabla \mathbf{u} = 0, \tag{2.3.20}$$

Note that we can absorb a constant part of the pressure gradient in the force if we transform the boundary conditions for the pressure adequately. This possibility is especially helpful in systems where one has parallel in- and outlets with a simple pressure difference between them, as one can then transform the problem simple homogeneous boundary conditions for the pressure.

Now finding the weak form of the Stokes equation by taking the inner product of Eq. (2.3.19) with a velocity test-function, and Eq. (2.3.20) with a pressure test-function adding them together, then integrating over space, using partial integration to get[30]:

$$\int_\Omega \nabla \mathbf{u} \colon \nabla \mathbf{v} + P\nabla\cdot\mathbf{v} + Q\nabla\cdot\mathbf{u}\mathrm{d}v + \int_{\Gamma_I} P(\mathbf{x})\mathbf{n}\cdot\mathbf{v}\mathrm{d}s(\mathbf{x}) \tag{2.3.21}$$
$$= \int_\Omega \frac{R^2}{2\lambda_D^2}\rho_e\nabla\varphi\cdot\mathbf{v} + \mathbf{f}_P\cdot\mathbf{v}\mathrm{d}v,$$

where Q is the pressure test-function, $\mathbf{v}$ is the velocity test-function and $\mathbf{f}_P$ is a constant of the pressure gradient meaning that the pressure P is slightly redefined. Note that we have flipped the sign of the pressure in order to get a symmetric equation. To implement the weak-form numerically, one needs second order elements, P_2-elements, for the velocity and first-order elements, P_1-elements, for the pressure, which is the so-called Taylor-Hood-elements. To solve the equation, we apply the above mentioned PCD precondition on the problem from the right side and solve the resulting system using the generalized minimal residual method (GMRES) Krylov subspace solver.

One could also consider less memory intensive alternatives by stabilizing the Stokes equation via an artificial compressibility which in turn allows for using the simpler $P_1 - P_1$ elements. The artificial compressibility will change the continuity equation in the following way Eq. (2.3.20)[33]:

$$\nabla\mathbf{u} - \varepsilon h^2 \nabla^2 P = 0, \tag{2.3.22}$$

where ε is a constant that controls the compressibility and should be chosen as small as possible in order to avoid compressibility errors yet so big that it suppresses pressure oscillations. h is the lattice size parameter, so one sees explicitly that the term vanishes to second order in space. The weak form of our problem becomes when Eq. (2.3.22) is used instead of Eq. (2.3.20):

$$\int_\Omega \nabla\mathbf{u}\nabla\mathbf{v} + P\nabla\cdot\mathbf{v} + Q\nabla\cdot\mathbf{u} - \varepsilon h^2 \nabla P\cdot\nabla Q\mathrm{d}v \tag{2.3.23}$$
$$+ \int_{\Gamma_I} P(\mathbf{x})\mathbf{n}\cdot\mathbf{v}\mathrm{d}s(\mathbf{x}) = \int_\Omega \frac{R^2}{2\lambda_D^2}\rho_e\nabla\varphi\cdot\mathbf{v}\mathrm{d}v$$

[28] https://fenapack.readthedocs.io/

[29] We have dropped the tilde over the dimensionless fields as all fields will be dimensionless in this section.

[30] Formally we have used the linearity of the differential operator along the Stokes theorem to get a higher dimensional equivalent

Now, in order to solve the discreet equation originating from this weak form, we have applied the following preconditioner:

$$b = \int_\Omega \nabla \mathbf{u} \colon \nabla \mathbf{u} + \nabla P \cdot \nabla Q \mathrm{d}v \tag{2.3.24}$$

along the FEniCS native "amg"(algebraic-multi-grid-preconditioner) and finally it was solved with the minimal residuum Krylov space solver. However, the method has not been used in the further study due to the compression error being too large in our initial tests.

Weak-form of the linearized Poisson-Boltzmann Equation

In order to get a good initial guess for the Poisson-Nernst-Planck equation, we have to solve the linearized Poisson-Boltzmann equation. Note that the linearization have been done for a binary symmetric monovalent ion-solution, but it is possible to extend it to more general chases. In Section 2.2.4 we have derived the Poisson-Boltzmann equation to have the following form:

$$\nabla^2 \varphi = \frac{2 q_e n^\infty}{\epsilon_r \epsilon_0} \sinh\left(\frac{q_e \varphi}{k_B T}\right), \tag{2.3.25}$$

Finding the dimension less form by using Table 2.1 and expanding in the potential around zero yields the none dimensional linearized Poisson-Boltzmann equation:

$$\nabla^2 \varphi = \frac{R^2}{\lambda_D^2} \varphi, \tag{2.3.26}$$

Now, in order to find the weak form version we multiply with a test function, then integrate over space and finally partial integrate which leads us to:

$$-\int_\Omega \nabla \varphi \nabla \psi + \frac{R^2}{\lambda_D^2} \varphi \mathrm{d}v + \int_{\Gamma_{CW}} \psi \nabla \varphi \cdot \mathbf{n} \mathrm{d}s = 0, \tag{2.3.27}$$

where ψ is the test function for the electric potential. Now we can use Eq. (2.2.20) to eliminate the electric potential from the boundary integral, hence getting:

$$-\int_\Omega \nabla \varphi \nabla \psi + \frac{R^2}{\lambda_D^2} \varphi \psi \mathrm{d}v + \int_{\Gamma_{CW}} \psi \frac{R^2}{2\lambda_D^2} \sigma_e \mathrm{d}s = 0, \tag{2.3.28}$$

where σ_e here is the dimension less surface charge, which is scaled with the constant $\tilde{z} q_e n^\infty R$.

With the weak form expression of the linearized Poisson-Boltzmann equation, we can now specify how we solved it. For preconditioner, we used the FEniCS native "hypre_euclid" which is a massively parallelized incomplete LU [31] decomposition from the HYPRE-library[32]. To solve the resulting linear system, we used the generalized minimal residuum Krylov space solver. It should be noted that when solving the Poisson type equation, there is an issue of fixing a gauge, however, this has not been a larger concern for us as we have always had a Dirichlet condition for grounding the potential hence setting a zero point.

Having found the electric potential from the linearized Poisson-Boltzmann equation one can use the relation given in Eq. (2.2.38) to get the ion-number densities. Note that in principle one should

[31] LU stands for Lower-Upper

[32] https://computation.llnl.gov/projects/hypre-scalable-linear-solvers-multigrid-methods/software

also Taylor expand ion-number densities around zero potential in order to get a consistent density. But keeping the exact form prevents the number density from becoming negative even if we leave the linear regime.

With a method to get an initial guess on the electric system, we will now discuss the Newton solver for the Nernst-Planck-Poisson problem.

Newton solver for the Nernst-Planck-Poisson problem

Again we want to find the weak form with only first order derivatives, but as the Nernst-Planck-Poisson problem is non-linear we have to linearize it first if we hope to solve it by a finite element method. To linearize we start by sing multiplying Eqs. (2.2.27) and (2.2.30) by appropriate test functions, adding them together and integrating over the domain [33]:

$$\begin{aligned} 0 = \int_\Omega \big[& \psi \nabla^2 \varphi + \psi \frac{R^2}{2\lambda_D^2} (n_+ - n_-) \\ & - c_+ \mathrm{Pe} \nabla \cdot (\mathbf{u} n_+) + c_+ \nabla^2 n_+ + c_+ \nabla \cdot (n_+ \nabla \varphi) \\ & - c_- \mathrm{Pe} \nabla \cdot (\mathbf{u} n_-) + c_- \nabla^2 n_- - c_- \nabla \cdot (n_- \nabla \varphi) \big] \mathrm{d}v \end{aligned} \tag{2.3.29}$$

where ψ is the test function for the electric potential and $c_+,\ c_+$ is the test function for the cation and anion number-densities respectively.

Using the integral in Eq. (2.3.29) can be seen as functional called $F(\mathbf{U})$, where $\mathbf{U} = (\varphi, n_+, n_-)$. We can linearize the equation by expanding $F(\mathbf{U})$ around some given $\mathbf{U}$ called $\mathbf{U}^0$. To first order, the expansion gives us what is essentially a Newton method for finding $\mathbf{U}$:

$$0 = F(\mathbf{U}^0) + \delta F(\mathbf{U})|_{\mathbf{U}=\mathbf{U}^0} + \mathcal{O}(\delta^2) \tag{2.3.30}$$

where $\delta F(\mathbf{U})$ is the functional derivative [34] , defined as

$$\delta F(\mathbf{U}) = \int_\Omega \frac{\delta F(\mathbf{U})}{\delta \mathbf{U}} \delta \mathbf{U} \mathrm{d}v, \tag{2.3.31}$$

where $\delta \mathbf{U}$ is the variation away from $\mathbf{U}^0$. Now calculating Eq. (2.3.31) explicitly in the chase of Eq. (2.3.29) gives:

$$\begin{aligned} \delta F(\mathbf{U})|_{\mathbf{U}=\mathbf{U}^0} = \int_\Omega \big[& \psi \nabla^2 \delta\varphi + \psi \frac{R^2}{2\lambda_D^2} (\delta n_+ - \delta n_-) \\ & - c_+ \mathrm{Pe} \nabla \cdot (\mathbf{u} \delta n_+) + c_+ \nabla^2 \delta n_+ \\ & + c_+ \nabla \cdot \left(\delta n_+ \nabla \varphi^0\right) + c_+ \nabla \cdot \left(n_+^0 \nabla \delta\varphi\right) \\ & - c_- \mathrm{Pe} \nabla \cdot (\mathbf{u} \delta n_-) + c_- \nabla^2 \delta n_- \\ & - c_- \nabla \cdot \left(\delta n_- \nabla \varphi^0\right) - c_- \nabla \cdot \left(n_-^0 \nabla \delta\varphi\right) \big] \mathrm{d}v \end{aligned} \tag{2.3.32}$$

[33] Note that we here use the convention that the differential operator only act on the object to their immediate right.

[34] Note that the functional derivative in the field of mathematics is called different things depending of the precise context. In the context of Banach spaces it is formally known as a Fréchet derivative and in more general setting it call a Gâteaux derivative.

Using the linearity of the differential operator along with the Stokes theorem on Eqs. (2.3.29) and (2.3.32), evaluating them in $\mathbf{U}^0$ and introducing the result in Eq. (2.3.30) gives:

$$
\begin{aligned}
0 = \int_\Omega \big[& -\nabla\psi\nabla\varphi^0 + \psi\frac{R^2}{2\lambda_D^2}\left(n_+^0 - n_-^0\right) \\
& + \mathrm{Pe}\nabla c_+ \cdot \left(\mathbf{u}n_+^0\right) - \nabla c_+ \cdot \nabla n_+^0 - \nabla c_+ \cdot \left(n_+^0 \nabla\varphi^0\right) \\
& + \mathrm{Pe}\nabla c_- \cdot \left(\mathbf{u}n_-^0\right) - \nabla c_- \cdot \nabla n_-^0 + \nabla c_- \cdot \left(n_-^0 \nabla\varphi^0\right) \big]\mathrm{d}v \\
+ \int_\Omega \big[& -\nabla\psi\nabla\delta\varphi + \psi\frac{R^2}{2\lambda_D^2}\left(\delta n_+ - \delta n_-\right) \\
& + \mathrm{Pe}\nabla\cdot c_+ \left(\mathbf{u}\delta n_+\right) - \nabla c_+ \cdot \nabla\delta n_+ \\
& - \nabla\cdot c_+ \left(\delta n_+ \nabla\varphi^0\right) - \nabla\cdot c_+ \left(n_+^0\nabla\delta\varphi\right) \\
& + \mathrm{Pe}\nabla c_- \cdot \left(\mathbf{u}\delta n_-\right) - \nabla c_- \cdot \nabla\delta n_- \\
& + \nabla c_- \cdot \left(\delta n_- \nabla\varphi^0\right) + \nabla c_- \cdot \left(n_-^0\nabla\delta\varphi\right) \big]\mathrm{d}v \\
+ \int_\Gamma \big[& \psi\nabla\left(\varphi^0 + \delta\varphi\right)\cdot\mathbf{n} - \mathrm{Pe}\left(c_+\left(n_+^0 + \delta n_+\right) + c_-\left(n_-^0 + \delta n_-\right)\right)\mathbf{u}\cdot\mathbf{n} \\
& + c_+\nabla\left(n_+^0 + \delta n_+\right)\cdot\mathbf{n} + c_+\left(n_+^0 + \delta n_+\right)\nabla\left(\varphi^0 + \delta\varphi\right)\cdot\mathbf{n} \\
& + c_-\nabla\left(n_-^0 + \delta n_-\right)\cdot\mathbf{n} - c_-\left(n_-^0 + \delta n_-\right)\nabla\left(\varphi^0 + \delta\varphi\right)\cdot\mathbf{n} \\
& - \left(c_+\delta n_+ - c_-\delta n_-\right)\delta\varphi\cdot\mathbf{n}\big]\mathrm{d}s,
\end{aligned}
\tag{2.3.33}
$$

Notethat the last term is of second order in δ and will therefore be dropped in the following, but it have allowed us to write all the boundary terms so the full solutions satisfy them U.

The above is the Newton method formulation of the Poisson-Nernst-Planck-problem, and we will use it to find solutions to the full Poisson-Nernst-Planck problem. The solution is found by solving Eq. (2.3.33) successively and after each step update $\mathbf{U}^0$ by:

$$
\mathbf{U}^0 = \mathbf{U}^0 + \delta\mathbf{U}, \tag{2.3.34}
$$

until L^2=norm $\delta\mathbf{U}$ becomes smaller that some tolerance meaning that U^0 have converged to U.

In order to make Eq. (2.3.33) ready for direct applications the boundary terms will have to be specified by using the ones introduced in Section 2.2.2. Let's take the boundary terms one by one, starting with the term for the electric potential:

$$
\int_{\Gamma_C W} \psi\nabla\left(\varphi^0 + \delta\varphi\right)\cdot\mathbf{n}\mathrm{d}s = \int_{\Gamma_C W}\psi\frac{R^2}{2\lambda_D^2}\sigma_e\mathrm{d}s \tag{2.3.35}
$$

where we used Eq. (2.2.20). The second term in Eq. (2.3.33) is zero due to the no-slip boundary condition Eq. (2.2.23) on the velocity field. Finally we have the following two flux terms which should vanish as we have a no-flux conditions:

$$
\int_{\Gamma_C W} c_\pm\nabla\left(n_\mp^0 + \delta n_\mp\right)\cdot\mathbf{n} \pm c_\pm\left(n_\pm^0 + \delta n_\pm\right)\nabla\left(\varphi^0 + \delta\varphi\right)\cdot\mathbf{n}\mathrm{d}s = 0 \tag{2.3.36}
$$

With the boundary terms simplified by introducing the prober boundary condition our weak form of

the Newton method becomes:

$$
\begin{aligned}
0 = \int_\Omega \big[& -\nabla\psi\nabla\varphi^0 + \psi\frac{R^2}{2\lambda_D^2}\left(n_+^0 - n_-^0\right) \\
& + \frac{1}{\mathrm{Pe}}\nabla c_+ \cdot \left(\mathbf{u}n_+^0\right) - \nabla c_+ \cdot \nabla n_+^0 - \nabla c_+ \cdot \left(n_+^0 \nabla\varphi^0\right) \\
& + \frac{1}{\mathrm{Pe}}\nabla c_- \cdot \left(\mathbf{u}n_-^0\right) - \nabla c_- \cdot \nabla n_-^0 + \nabla c_- \cdot \left(n_-^0 \nabla\varphi^0\right) \big]\mathrm{d}v \\
+ \int_\Omega \big[& -\nabla\psi\nabla\delta\varphi + \psi\frac{R^2}{2\lambda_D^2}\left(\delta n_+ - \delta n_-\right) \\
& + \frac{1}{\mathrm{Pe}}\nabla \cdot c_+ \left(\mathbf{u}\delta n_+\right) - \nabla c_+ \cdot \nabla\delta n_+ \\
& - \nabla \cdot c_+ \left(\delta n_+ \nabla\varphi^0\right) - \nabla \cdot c_+ \left(n_+^0 \nabla\delta\varphi\right) \\
& + \frac{1}{\mathrm{Pe}}\nabla c_- \cdot \left(\mathbf{u}\delta n_-\right) - \nabla c_- \cdot \nabla\delta n_- \\
& + \nabla c_- \cdot \left(\delta n_- \nabla\varphi^0\right) + \nabla c_- \cdot \left(n_-^0 \nabla\delta\varphi\right) \big]\mathrm{d}v \\
+ \int_\Gamma \psi\frac{R^2}{2\lambda_D^2}\sigma_e \mathrm{d}s.
\end{aligned}
\tag{2.3.37}
$$

In order to get fast and robust converges for a Newton method one needs a good initial guess to linearize around at the beginning. In our case we can use the solution we got from the linearized Poisson Boltzmann equation, as an initial guess and as long as we stay in the linear regime it works quite well. To solve the linearized equation given in Eq. (2.3.37) we have used the FEniCS "GEMRES" (generalized minimal residuum) and its default preconditioning which is a Jacobi precondition combined with an incomplete LU precondition. The Jacobian based preconditioners yield fairly robust solvers, however, it turns out for the Nernst-Planck-Poisson problem that it is only working for moderately big systems. As a consequence we have not been able to run big 3 dimensional systems as this requires better preconditions to get proper converges, which is a non-trivial task to develop and beyond the scope of this work. Finally, it should be mentioned that there is no guarantee that a newton scheme will converge in general but in our case, it has been rather successful with the provided the initial guess.

2.3.4 Mesh generation

Our simulations have been carried out in straight and undulated channels in both 2 and 3-dimensions, a more precise description of the geometries will be postponed to the discussion of the numerical results, as we in this section is mainly interested in the mesh generation.

For the mesh for the straight channels one can use structured triangular/tetrahedron discretizations that are natively implemented in FEniCS, and is called `RectangleMesh` and `BoxMesh` for 2 and 3-dimensions respectively. Structured discretization also allows for easy control over the resolution and ensures that the mesh was periodic which is needed in order to insurer better numerical stability.

For the more complex undulated channels there is no standard function in FEniCS that can be used to generate such meshes. As further constrained we need periodic meshes in some of the directions which means that the mesh generation are a bit tedious as this not a generally supported feature in most meshing software. One could take different approaches for generating the periodic undulated channels as they in our case have a mirror symmetry, but if the method should be generally valid one have to define the surface mesh manually in such a way that the faces of the mesh that are periodic can

be mapped trivially to each other. We used the Triangle[69] along the Python package MeshPy[35] to make the surface mesh such that it had the qualities needed. With the surface mesh from MeshPy, we used the meshing tool TetGen[70] to mesh the volume with homogeneous tetrahedron size. Besides ensuring the periodic properties manually defining the surface mesh also has the advantage that one can avoid an unnecessary rough surface that can be the result of meshing surfaces by more automatic methods utilized by programs like CGAL.

Now, with all the components needed in order to simulate electrohydrodynamics let us turn to the section where we describe the results of our simulation in the advertised geometrics discussed above.

2.4 Numerical Results

With the technical details of the program covered and some theoretical predictions of macroscopic quantities introduced. We will now turn our attention towards the use of the program. The first step will be to validate that the code in fact produces results comparable to the different theoretical predictions. After the validation, we will present the found effect of undulating one of the walls of the channel with different amplitudes

2.4.1 Validation

In order to validate the numerical scheme presented in Section 2.3, we have first conducted simulations in 2-dimensional channels and compared the results to theoretical predictions. This was done in two geometries: one long channel to avoid any boundary conditions to interfere with the results and one short channel as to keep the system size small enough so the solver could obtain convergence in the 3-dimensional chase. A sketch of the channel can be found in Fig. 2.4.1

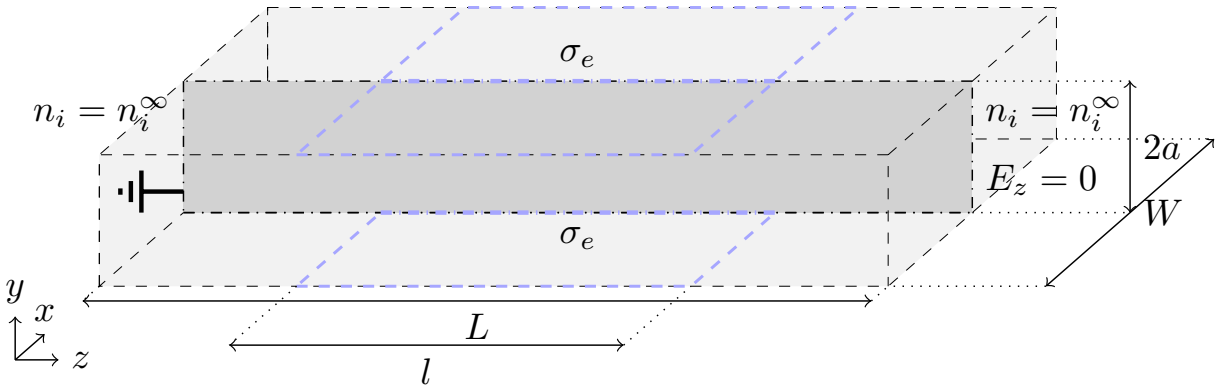

Figure 2.4.1: The fully draw par of the fisher is the 2-dimensional geometry where the charged walls is made with blue and have the surface charge of σ_e, the ends of the channel we have in the indicated boundary condition, the dimension is given by L the total length o the channel, l the charge path of the channel and a half width of the channel. The dashed part of the figure is the 3D extension and should be understood as a periodic dimension it has the width of W.

The parameters that were chosen in order to non-dimensional the Stokes-Poisson-Nernst-Planck problem is given in Table 2.2. The long and short channel have the length of respectively $L = 160R$

[35] MeshPy, `https://documen.tician.de/meshpy/`

Simulation Parameters	Value
n^{∞}	$[6.691 - 240.8] \times 10^{20}\#/\mathrm{m}^3$
ζ	$-51.34\mathrm{mV}$
R	$96\mathrm{nm}$
a	$288\mathrm{nm}$
T	$298\mathrm{K}$
D	$1.0 \times 10^{-9}\mathrm{m}^2/\mathrm{s}$
k_B	$1.38 \times 10^{-23}\mathrm{J/K}$
$\epsilon_r\epsilon_0$	$8.854 \times 10^{-23}\mathrm{C/Vm}$
μ	$1.003 \times 10^{-3}\mathrm{Pa\ s}$
q_e	$1.602 \times 10^{-19}\mathrm{C}$
z	1
$\frac{\partial P}{\partial z}$	$1.0 \times 10^{7}\mathrm{Pa/m}$
τ	1.0×10^{-5}

Table 2.2: The simulation parameters, note that interval for the number-density is not cover equidistant in the number-density, but rater in the Debye length.

and $L = 40R$.

The macroscopic quantities we have been interested in the electro-viscosity μ_e and the streaming potential V_{str}. To measure the electro-viscosity, we solved the Stokes equation without considering the electric effects. This gave us the mean velocity flux along the z-axes by integrating the velocity field's z-component. Then we repeated the numerical experiment including the electric system for different values of inlet number-density and extracted the resulting mean velocity flux as in the electric neutral chase. Mean velocity flux was calculated from simulation by:

$$Q_z(\kappa a) = \frac{1}{L}\int_{\Omega} u_z(\kappa a)\mathrm{d}v, \tag{2.4.1}$$

where L is the total length of the channel and $Q_z(\kappa a)$ is the total z-flux across the channel for a given value of κa. Note that $\kappa a = 0$ corresponds with the fluid being electrically neutral. Now the following ratio would give the electro-viscosity in the infinite chase:

$$\frac{\mu_{e,h}}{\mu} = \frac{Q_z(0)}{Q_z(\kappa a)} \tag{2.4.2}$$

where the subscript h denote that only half of the tube is charged. To make a direct comparison to the theoretical predictions we will have to scale the found electro-viscosity as it should be tied to the amount of the channel that is charged:

$$\frac{\mu_e}{\mu} = \frac{1}{0.5}\left(\frac{\mu_{e,h}}{\mu} - 1\right) + 1 \tag{2.4.3}$$

where the division with one half is due to the fact that only half the channel was charged.

The steaming potential was measured by the performance of the following integral over electric-potential found by the numerical simulations:

$$\frac{V_{str}}{l} = \frac{\int_{\Gamma_{\mathrm{outlet}}} \varphi \mathrm{d}s}{l\int_{\Gamma_{\mathrm{outlet}}} \mathrm{d}s} \tag{2.4.4}$$

Note that we have divided with the length of the charged part of the channel in order to compare the results from both the short and long channel as the streaming potential as given in Eq. (2.2.59) scales linearly with length of the charged part for the channel.

The last thing we have measured is the ζ-potential at the center of the charged region and it was measured in all the simulations to be approxemately $\zeta = -45.2\mathrm{mV}$. This value is lower than the specified, but it should be noted that it was imposed implicitly through the Grahame equation. Furthermore, as we are both on the edge of linearity regarding the Poisson-Boltzmann equation and in a different geometry than where Grahame equation is an exact relation this should not be surprisingly. The measured values for the ζ-potential have been used to produce the theoretical curves for both the streaming potential and the elector viscosity.

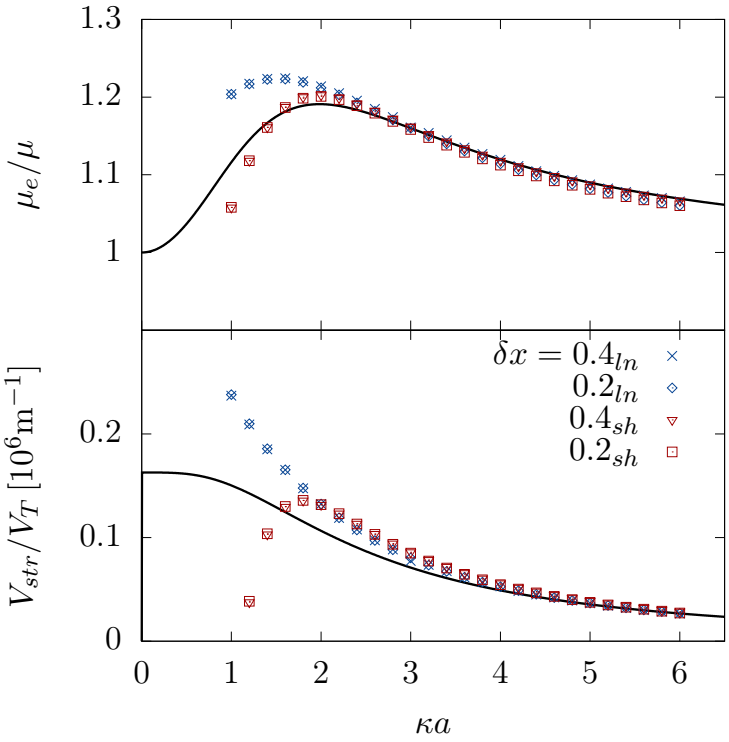

Figure 2.4.2: Top: The solid line denote the analytical result for the electro-viscosity, Eq. (2.2.63) with $\zeta = -45.2\mathrm{mV}$. The blue and red points denote the long and the short channels respectively, the legend further specifies the resolution. The measurements of the electro-viscosity were done as presented in the text. Bottom: The solid line denote the analytical streaming potential per length of channel, Eq. (2.2.59) again with $\zeta = -45.2\mathrm{mV}$. The blue and red points denote long short channels respectively, the legend further specifies the resolution. The measuring technique was the one described in the text.

The measured electro-viscosity and stream-potential in the 2-dimensional channel can be found in Fig. 2.4.2 along with the theoretical predictions. We see the measured quantities coincidence more or less with the theoretical values of κa above 3 for both channels, and that seems to be valid even though we have a surface potential on the limit of where the linearized Poisson-Boltzmann equations should hold. However, for values of κa below 3 we begin to see some different behavior for the two lengths.

The difference between the two lengths of channels can be attributed to the fact that the inlet for the short one is only a couple of Debye length long for $\kappa a = 1$, leading to an accidental bias voltage, inducing the drop in streaming-potential and electro-viscosity. Meaning there have de facto been introduced an uncontrolled electro-osmosis due to the finite size of the computational domain,

this might also break the electric-flux condition that was central for the derivation of Eqs. (2.2.59) and (2.2.63).

For the long channel, the difference signals a theoretical break down of the linearized Poisson-Boltzmann equation for the strongly interacting double layers. In order to capture the effect of overlapping double layers, one will have to consider the full nonlinear Poisson-Boltzmann equation and redo the calculation of section Section 2.2.4, under such conditions. Such calculations would rely heavily on numerical methods as the solution to the Poisson-Boltzmann equation in a channel is only known as implicit relations of elliptic integrals as can be found in [79, pp. 67]. Furthermore, one could imagine the inlet and outlet from the charge region become more prominent as the Debye length increases. To validate how our code works in 3 dimensions as well we ran the simulation of the same

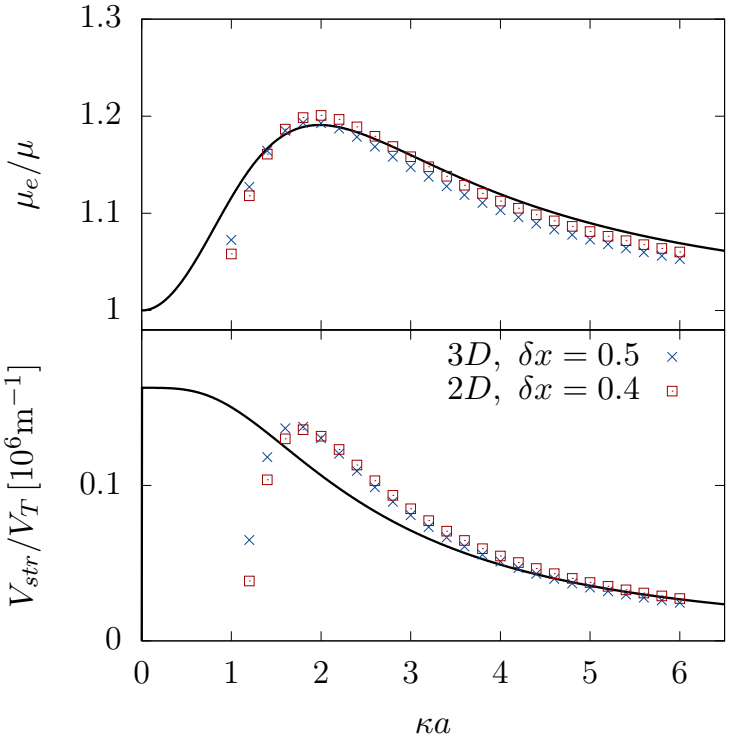

Figure 2.4.3: Top: The solid line denote the analytical result for the electro-viscosity, Eq. (2.2.63) with $\zeta = -45.2\mathrm{mV}$. The point is measurements of the electro-viscosity from the simulations and the legend gives their origin. Bottom: The solid line denote the analytical result for the stream-potential, Eq. (2.2.59)S with $\zeta = -45.2\mathrm{mV}$. The point is measurements of the stream-potential from the simulations and the legend gives their origin.

channel in 3 dimensions, hence we just added an extra cyclic dimension transverse to the flow as described in Fig. 2.4.1. The transverse dimension had a width of $= 1R$ The results for this simulation can be found in Fig. 2.4.3 and one sees that the 3-dimensional realization produces the same results with some minor differences that can be attributed to the slightly lower resolutions and to numerical errors.

However the 3-dimensional code seem to correspond to the theoretical predictions, so with this validated code, we can now study the effects of having a non-uniform channel. Further details on the validation of the solver can be found in Appendices A and C where it is compared to a time-depended scheme.

2.4.2 Effects for an Undulated Surface

As channel flow described above is highly idealized and does not depend on the third dimension due to symmetry, we would like to add some complexly to the geometry in order to break this. This will allow us to study of the electric effects on channeling and the general redistribution of the flow in complex geometries. In order to achieve this, we have to add an undulated surface at the bottom of

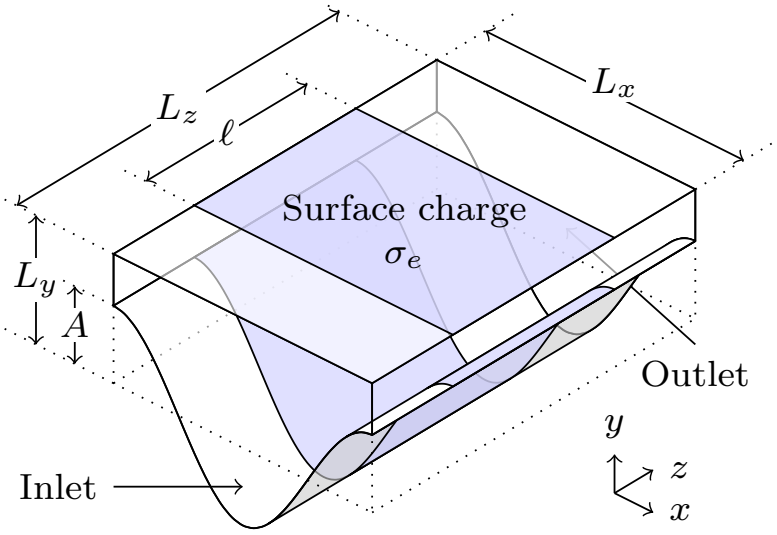

Figure 2.4.4: Schematic set-up of the model system. The inlet, charged-surface, and outlet areas (see text) are indicated. The x-direction is periodic. Note that the dimensions are not to scale.

the channel as shown on Fig. 2.4.4, which clearly breaks the symmetry along the x-direction and will of course change the flow due to the change in geometry. More precisely the top wall was placed at $y = L_y$ and spanned the interval $(x, z) \in [0, L_x] \times [0, L_z]$, the y-position of undulated surface, the bottom wall, was given by the following x-dependent function:

$$h(x) = A \cos\left(\frac{2\pi x}{L_x}\right), \tag{2.4.5}$$

the $x-$ and $z-$coordinate spanned the same interval as the top plane. Surface charge was placed in a band on both walls in the middle of the channel so the inlet and outlet was half the length of l, furthermore l was half the length of L_z. In the simulations the four lengths was set to $L_x = 12R$, $L_y = 6R$, $L_z = 40R$ and $A \in [0R, 3R]$. Finally, please note that in order to compare the simulation with the straight channel we have used the average width of the channel as $a = 3R$.

With in the defined geometry we would like to measure the asymmetry in th flow and eventually compare the charge and none-charge reliziation, so we need to define a measure of asymmetry. This is done in the following way, first we define some domains to integrate the flow over:

$$\Omega_t = [0, 12R] \times [-3R, 6R] \times [15R, 25R], \tag{2.4.6}$$
$$\Omega_y = [0, 12R] \times [3R, 6R] \times [15R, 25R], \tag{2.4.7}$$
$$\Omega_x = [-3R, 3R] \times [-3R, 6R] \times [15R, 25R], \tag{2.4.8}$$

Note that Ω_y is defined in such a way that it is constant and equals half the channel cross section for A's smaller than 3. The next step is to find the z-component of the flux through in the defined regions:

$$Q_{z,i}(A, \kappa a) = \frac{1}{10R} \int_{\Omega_i} u_z \mathrm{d}v, \quad i \in \{t, x, y\}. \tag{2.4.9}$$

This flux can now be used to define what we will call the absolute asymmetries, $\Theta_x(A, \kappa a)$ and $\Theta_y(A, \kappa a)$:

$$\Theta_i(A, \kappa a) = \frac{Q_{z,i}(A, \kappa a)}{Q_{z,t}(A, \kappa a)}, \quad i \in \{x, y\} \tag{2.4.10}$$

The two absolute asymmetries is both defined such that they equals $\frac{1}{2}$ in a straight channel. The changes of the absolute asymmetries due to the amplitude A have be estimated and to linear order in the amplitude A the $\Theta_y(A, \kappa a)$ should be constant while $\Theta_x(A, \kappa a)$ is given as[36]:

$$\Theta_x^{th}(A, 0) = \frac{1}{2} - \frac{6AL_x}{2\pi^2 L_y^2}\left[1 - \frac{1}{\cosh\left(2\pi\frac{L_y}{L_x}\right)}\right] : \tag{2.4.11}$$

We have plotted the numerical results for the absolute asymmetries as defined in Eq. (2.4.10) and

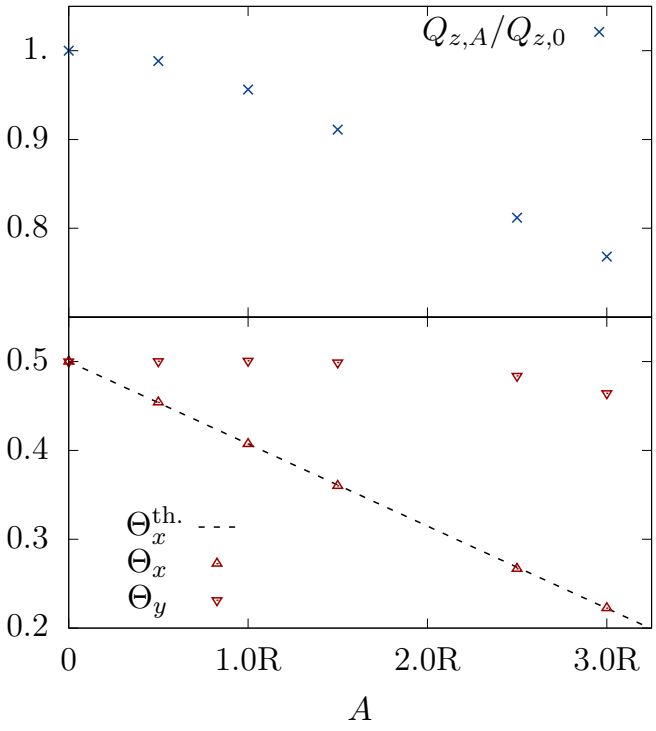

Figure 2.4.5: Top: Flow rate through the undulated channels as a function of amplitude A, in units of the flow rate in the flat channel $A = 0$ at $\kappa a = 0$ note that form an symmetry argument the slop at $A = 0$ should vanish. Bottom: the absolute asymmetry of the flow in the channel as a function of amplitude A at $\kappa a = 0$, the linear dependences of Θ_x on A is in good agreement whit $\Theta_x^{th\cdot}$ found in Eq. (2.4.11)

compared it against Eq. (2.4.11) in Fig. 2.4.5 along the $Q_{z,t}(A, \kappa a)$'s observed dependence on A.

In order to quantify the change in the asymmetry due to the surface charge we compared to the none-charge by introducing the relative asymmetries:

$$\theta_i(A, \kappa a) = \frac{\Theta_i(A, \kappa a)}{\Theta_i(A, 0)}. \tag{2.4.12}$$

Before presenting the results for the relative asymmetries of the charged undulated channel, let us first discuss the effect on the electro viscosity and the streaming potential. The electro viscosity and the

[36] The calculation can be found Appendix A in the articles appendixes C (not the appendixes C of the thesis)

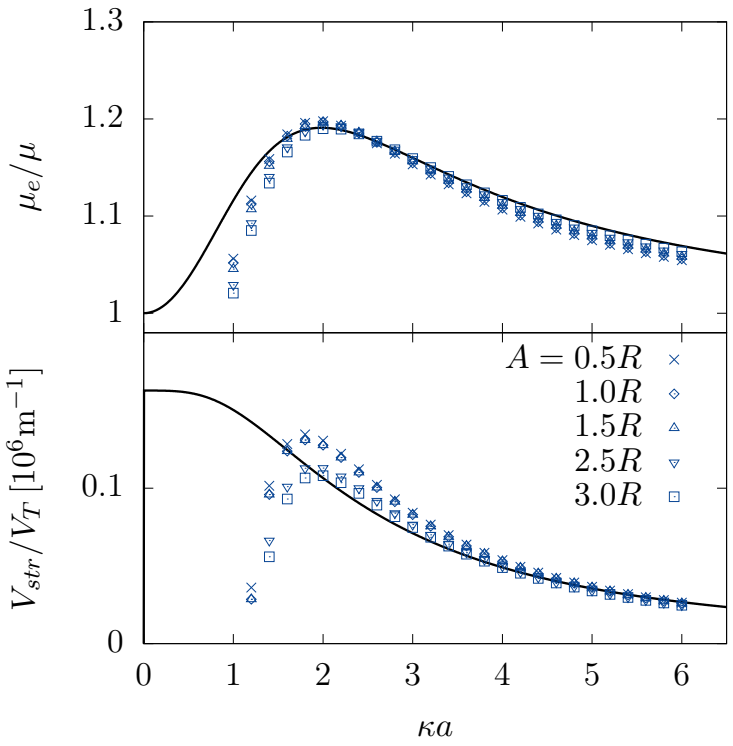

Figure 2.4.6: Simulation in channels as described in Fig. 2.4.4 and the dimension given in the text and A is given in the legend. Top: The electro-viscosity does not seem to be impacted a lot on a global but it is worth noting that for increasing amplitude the one sees a slight decrease for small values of κa. Bottom: The streaming potential seems to be more impacted by the change of amplitude; this could be due to the overlap of double layers in the narrow regions leading to stronger non-linear effects but also more leaking to the boundary.

streaming potential have been plotted for the different amplitudes in Fig. 2.4.6, and we see no major change of either of them. There is however a small effect that can be seen in the low κa limit and is properly linked to the narrow regions of the channel. This is due to a stronger leak of the double layer to the boundary because of strong interactions between the double layers in this region. The two relative asymmetries for the different amplitudes can be found in Fig. 2.4.7. The θ_y for smaller amplitudes do not change significantly however as amplitude increases one see a small drop due to the boundary layers in the narrow section interacting stronger than the one in the confined region in the bottom of the channel. A much larger effect can be seen on θ_x as it is only measured over the confined region where one would expect the effects to be biggest. We observe an enhanced channeling of the flow on a mean-field level. To get a more local notion of a decrease in the flow we will visualize this for the channel cross section. Such a local measure for flow reduction can be found in different ways: either one could simply subtract the charged flow from the non-charge flow or one could divide the two. However, the absolute difference in the flow does not illustrate how the flow is redistributed in the channel. For that one needs the relative difference in the flow. In order to measure the relative difference, we printed 40 z transverse slices of the z-component of the velocity in the region $z \in [12.5R, 27.5R]$, which is well within the charged region and then found their average them. Such average flow profiles in the charge region were measured both for a none charge flow and for an inlet number density of $6.022 \cdot 10^{21} \#/\mathrm{m}^3$ meaning $\kappa a = 3$. Finally, we divide the charged profile with the non-charged. The plot of this field can be found in Fig. 2.4.8 for four of the amplitudes. We see for the larger amplitudes $A \in [2.5R, 3R]$

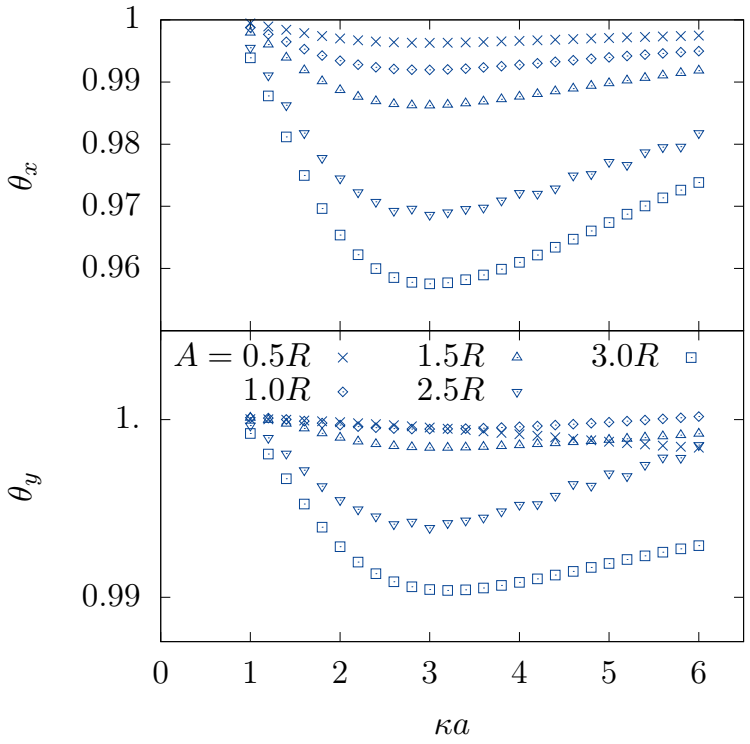

Figure 2.4.7: Top: Plot of θ_x we set that the there is a incensed damping of the flow in the narrowing of the channel which means that effectively the channeling of the amplitude gets argument by the electric effects. Bottom: Plot of θ_y. We see that for low amplitude it is more or less constant and an effect only becomes pronounced as the amplitude increases enough to make a narrow region in the bottom of the channel.

that the flow can locally change with up to $10 - 15\%$ in extended regions of the more constricted parts of the channels, and the flow in the center region is in comparison only reduced with less than 5%. For the smaller amplitudes $A \in [0.5R, 1R]$ we that locally change is confined to a thin layer near the walls. This means that the regions with already low permeability will exclude flow even more. Note that due to a "0 over 0" phenomenon the relative field becomes filled with artifacts near the edge.

With this, we conclude the section regarding the numerical results and turn to the discussion of where such results could be of importance.

As a concluding note, all the 3-dimensional simulation was done on our in-house server with 2 64 bit CPUs, 28 cores ad 2.6 GHz and 512 Gb of RAM. On this hardware the simulations took around 1-2 hour for each the geometry for each of the ion-number densities, meaning a total computational time of the order of 10^2 hours. The 2-dimensional simulations were done on a desktop computer in a matter of hours.

2.5 Discussion

Off course, our study had some numerical shortcomings as we were not able to increase the number of degrees of freedom in the finite element scheme due to an ill-preconditioned Poisson-Nernst-Planck problem. As good preconditioning is not a simple endeavor to construct in general, it has not been pursued further but it should be of importance if the one whats to continue developing the method. It should also be noted that one might be able to avoid the preconditioning problems by using an

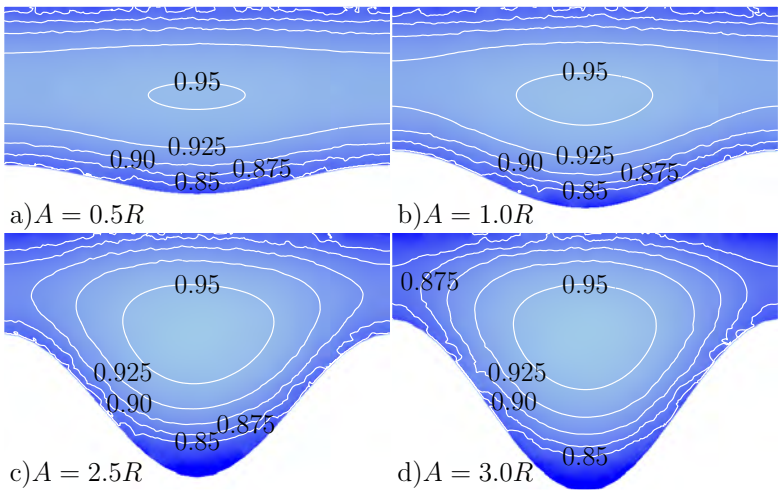

Figure 2.4.8: All the figures show the relative charge flow field when compared to changeless flow at $\kappa a = 3$ the measurement was done as described in the text. In both a) and b) we do not see a major increase in channeling but there is an indication of some in the constricted regions. Differently in both c) and d) we see that the flow get more constricted to the center region and that there is at 10% reduction of flow in the narrow regions (side gab and in the bottom of the channel)

implicit time integrated method with non-resolved time steps, such methods could be based on what was used the validation presented in the supplementary-material found Appendix A [37]. The limits on finite element system size meant that we could not have the in- and outlet length required to avoid the boundaries to interfere with the found solution for the lower number-densities.

Besides such oblivious limitation of our numerical method, there is also more subtle details in the studies that must be discussed. Let us first consider the scan in κa, where we used the number density as the scanning parameter which for the streaming potential lead to a discontinuity at $\kappa a = 0$. This discontinuity could be avoided if the scan had been done by changing the channel width instead, like was the case for Mansouri et. al.[44], who did similar studies just in an axially symmetric pore but with varying pore radii.

Another less obvious weakness for both the theoretical expression for electro viscosity and streaming potential Eqs. (2.2.59) and (2.2.63) respectively is that they are derived from the linearized Poisson-Boltzmann equation, hence especially for strongly interacting electric double layers this might break down. Such breakdown of the linear theory might be a part of the reason why our results in the long channel does not match, another reason could be that the equilibrium hypothesis used to derive the Poisson-Boltzmann equitation have broken down. While the effect of the departure from equilibrium might be difficult to model without solving the full system, the departure from the linearized Poisson-Boltzmann equation should be feasible to study. A starting point for introducing non-linear effects from Poisson-Boltzmann equations could be to use the implicit solution to the equation found by [79, pp. 67], along with some numerical methods to obtain the electron viscosity and streaming potential from this.

With some technical issues addressed let us also discuss the effects of electro viscosity in context of geological and industrial settings. Under the geological conditions found in porous rocks such as limestone and chalk the effect of electro-viscosity can affect the distribution of flow. Such change could have a rather big influence on precipitation or dissolution and might lead to a faster closing of pores or stronger tunneling depending on specific parameters chosen. In industrial settings, the increase of flow resistivity can be of great importance in many applications. For an example in ion-selective membranes for water treatment, it can be used to study how to avoid the necessary pressure

drop due to inhomogeneity of the membrane pores. But it might also play a role in understating non-homogenius porous catalysts and how to optimize them by avoiding or utilizing electro-kinetic effects.

2.6 Conclusion and Outlook

By using numerical tools we were able to show that electric effects within the Poisson-Nernst-Planck-Stokes equation play an important role in the redistribution of flow in an undulated channel. Hence we have seen that not only can electro viscus effects reduce the flow rather dramatically in our case $\sim 20\%$ but they can also lead to macroscopic redistribution of around $\sim 5\%$ and a local effect that can be in the order of $\sim 10\%$. The effects of electro viscus channeling are increased by increasing the amplitude, at least within the range we studied. It should be noted that the flow asymmetries might be underestimated due to only half of the channel being charged, furthermore one should not expect a linear relationship in the charge fraction as for the electro viscosity. Even though such simplified geometry as the undulated channel might not be found Nature the results for it can still be used to get an understanding of the effects in more elaborated fracture apertures of porous media hence it can be thought of as a first approximation to more complicated geometries. This means that the electro-viscous effects can lead to stronger channeling also in such geometries, however in order to quantify the effects more precisely one would have to simulate bigger systems. This high lights the insufficiencies in our numerical solver, and what should be the main future challenge namely to make the solver efficient for larger systems, by developing better preconditioning. The possibility of larger system size also makes it possible to handle in- and outlet in a more proper way and to study a broader range of Debye lengths.

Finally, it would be rather interesting to couple the Poisson-Nernst-Planck-Stokes problem to some equation that governs precipitation/dissolution of the geometry, to study what effects the electric forces have on such phenomenon.

Chapter 3

Two Phase Electrohydrodynamics

This chapter will be dealing with two-phase electrohydrodynamics as the title suggests. The model, it's theoretical and implementation in FEniCS can be found in the attached paper, see, Appendix D along with a study of converges and validation of the numerics. So this chapter will concern some phenomenology of electrowetting in none trivial geometries, and the numerical modeling of this with *Bernaise*, more quantitative work on electrowetting see the paper in Appendix B.

3.1 Motivation

As the document in Chapter 2 shows we have worked quite a lot with one phase electrohydrodynamics, and through this work got a general understanding of related phenomenon. However, many of the effects of electrohydrodynamics in one-phase fluids are mainly damped dynamics or introduce extra flow resistance as was the case for electro-viscosity. On the contrary one could imagine many exotic effects of electrohydrodynamics in a set up consisting of two immersible phases with different electric properties. A particular example where such phenomenon can be important for the dynamics is a water-oil interface in a porous media if there are ions dissolved in the water phase and the confining pore is charged. The idea of studying such a setup came from some none published numerical experiments by Rastin Martin [1] and Marek Krzysztof Misztal [2]. In their experiments, they investigated if it was possible to expel a partial none-wetting fluid from a dead-end pore with a partial wetting fluid under a sheer flow. From this numerical work, they saw that it was not possible to expel the droplet from the dead-end pore by changing the contact angle up to $45\,\mathrm{deg}$ from neutral.

Expelling of oil droplets for pores is common to observe in nature, fx in later phases of oil recovery, and one could speculate that might play a role in such cases [19]. The effects of electrohydrodynamics on wetting phenomenons have been noted as early as 1875[38] and have been reviewed in recent years due to advances of microfluidics [13], variable-focus lenses[29] and electronic paper[20, 50].

The structure of the rest of the chapter starts with a discussion the phenomenology of electrohydrodynamics and the origins of electrowetting, then we present the setup of some numerical experiments and the outcome of the resulting simulations. We will end by discussing what could be done in future studies and which problems need to be addressed.

[1] A Ph.D. form our group at The Niels Bohr Institute doing two-phase lattice Boltzmann simulations with none trivial wetting.

[2] At the time of writing Assistant Professor at The Niels Bohr Institute, doing two-phase lattice Boltzmann simulations with none trivial wetting.

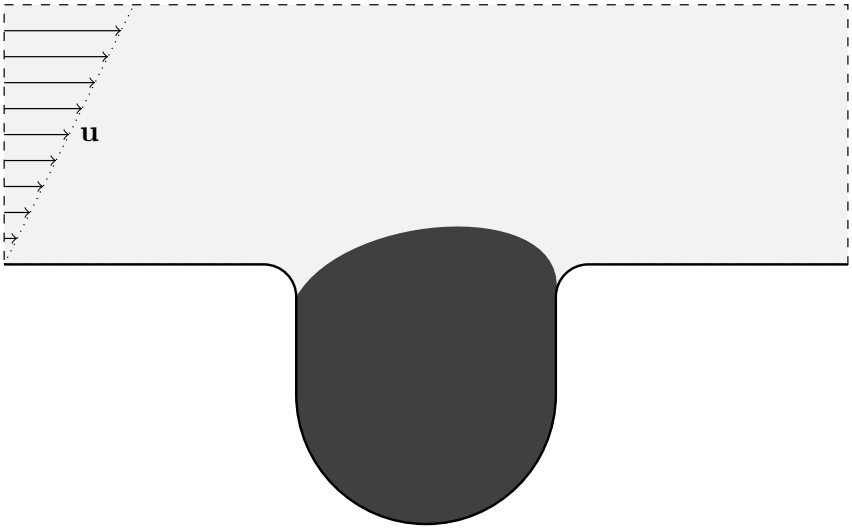

Figure 3.1.1: A shear flow of water moves across the inlet of a non-charged micropore filled with oil. Even if the water is partial wetting the droplet is not pushed out due to capillarity but is only distorted.

3.2 Theory

This section will deal with the phenomenology of intrusion due to electricwetting, for a discussion of the model for two-phase electrohydrodynamics see Appendix B, where it is introduced in the first part of the paper.

3.2.1 Phenomenology

Two phase flow have a rich dynamic in confined geometries even without surface charge effects [36, 66]

However some dynamics of fluid can be affected by electrostatic forces leading to intrusion near a charged wall, efficiently increasing the apparent wetting angle and preventing stagnating of the contact line, this can all be modeled by electrohydrodynamics with two phases.

Electric Static Effects on Intrusion

Our initial motivation for the studying of two-phase electrohydrodynamics was to study if it made expelling the oil droplet in Fig. 3.1.1 with the help of electrostatic effects. The reasoning was that as oil and water have rather different electric and solvent properties, water being a rather good solvent to dissolute simple salts where oils are typical not. The difference in their properties as solvents means that the Debye length in the two fluids can easily differ in the two phases by a substantial amount. In particular the Debye length in water will typically be smaller than the one in oil, even if the relative permittivity of oil is typical an order of magnitude smaller than that of water[3]. Such difference in Debye length means that the electric force density on the water near a charge wall is larger than the one on oil a pointing towards the none screened surface charge . This localized force will then lead to intrusion of a thin film along the wall if the surface tension is sufficiently small and the force can in

[3]Note that the relative permittivity of oil can vary quite a lot depending on the precise composition but it is typical in the range: $\epsilon_r \sim 2 - 10$

some limits lead to oil phase gets displaced away from the wall, for an illustration of such a process in dead pore see Fig. 3.2.1.

A similar effect can also be anticipated to have an effect on intrusions in porous media, as it can have a large effect on destabilizing stagnated contact lines. This will in practice mean that it can speed up pressure driven intrusion or even expel plugs that normally would stay due to being stabilized by a Poisson pressure.

3.3 Numerical Setup

To get a preliminary confirmation that the numerical method developed in *Bernaise* has made it feasible to study electric effects on intrusion we set up two model geometries and ran simulations in these. The two model geometries where: a dead-end pore see Fig. 3.3.1 , and a pore throat see Fig. 3.4.2.

Both geometries were set up within the *Bernaise* problems submodule and can be found in the git repository under the names `"snoevsen.py"` for the dead-end pore and `"hourglass.py"` for the pore throat. The input mesh for the two problems was made using the "mshr"[4] tool which is developed for FEniCS and specific script can be found in the folder: `"/utilities/mesh_scripts"` and can be made by typing the following in the terminal:

```
$  python generate_mesh.py mesh=...
```

Where the `"mesh"` is chosen to be: `"snoevsen"` or `"hourglass"`. If one need to use some of the further functionality the `"generate_mesh.py"` can be followed with a `"-h"` instead of the `"mesh"`.

The two simulations were run with the model parameters found in Table 3.2, which are given in the *Bernaise* units. Note that the subscripted 1 corresponds to the phase called I in the fingers and 2 to II.

3.3.1 Boundary and Initial Conditions

The boundary and initial conditions on the two geometries are indicated on their schematics but will be described hereafter in full detail. For the dead-end pore Fig. 3.3.1 boundary conditions are given so that The x-direction of the geometry is periodic, meaning that edges marked with dashed lines are identified to each other. At the top plane which is indicated with at dotted-dashed line, a sheer flow is applied to the velocity field so the $u_x = u_{top}$ and furthermore a constant number-density for the two ion types are set as $c_i = c_0$ and the electric-potential is grounded $V = 0$. At the bottom of the channel marked with a fat blue line, a no-slip condition is applied for the velocity field, a no-flux condition for the number-densities, and a flux condition is set for the electric potential to match the surface charge. Finally, for the phase field has a no-flux condition at all of the none periodic boundaries along a neutral contact angel, and the pressure field is fixed at one point to handle the gauge freedom.

For initial conditions the pressure, velocity and electric fields is set to zero over the entire domain, the phase field is initialized so that the hole of the dead-end pore is filled with phase I corresponding to $\phi = 1$ by the following function:

$$\phi = -\tanh\left(\frac{\max(y, \sqrt{(x - Lx/2^2} - 2R)}{\sqrt{2}\varepsilon}\right) \tag{3.3.1}$$

[4] https://bitbucket.org/fenics-project/mshr

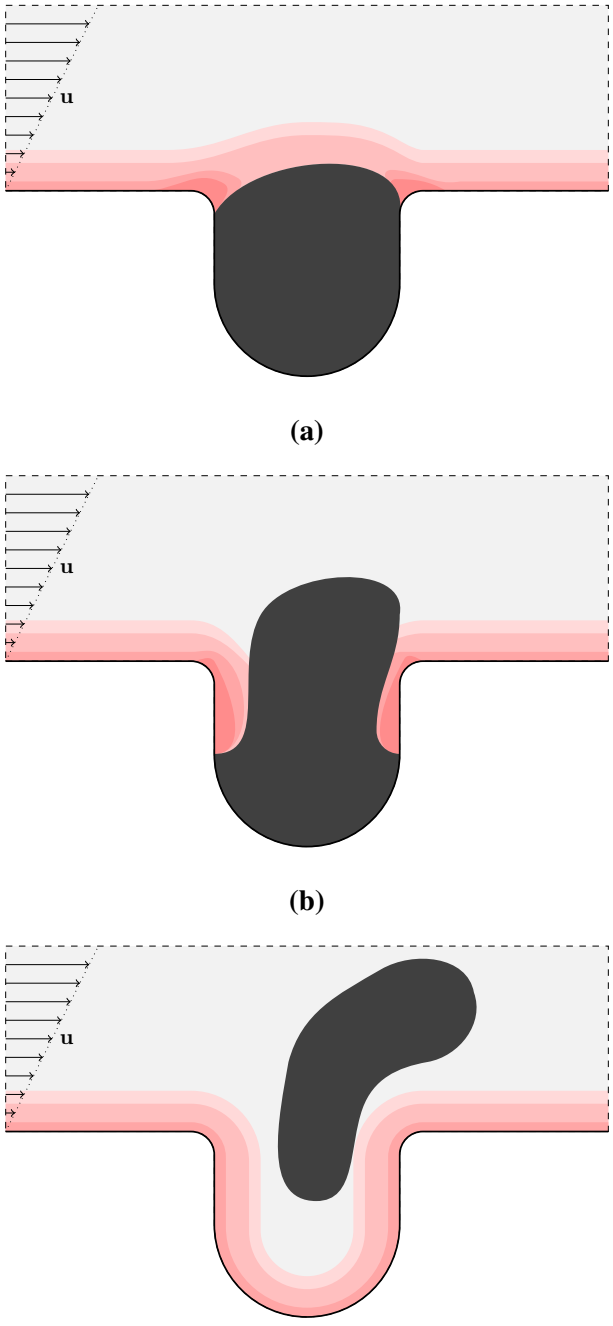

Figure 3.2.1: (a) The same geometric configuration as in Fig. 3.1.1 however, in addition, there is a surface charge at the pore-walls. This surface charge leads to an electric double layer being form in the water phase. (b) The same pore but at a later sated, now a water film is intruding along the pores walls due to electrostatic effects (electro-wetting). (c) The water intrusion is completed and the oil has been pushed out of the pore.

Name	Simulation Parameters	"Dead-end"	"Throat"
Length	L_x	3.0	6.0
Hight	L_y	1.0	2.0
Total Time	t	20	20
Radius	R	0.3	0.3
Time step	dt	0.01	0.02
Resolution	res	120	120
Interface thickness	ε	0.02	0.02
Phase field mobility	M_0	$2.5 \cdot 10^{-6}$	$2.5 \cdot 10^{-6}$
Surface tension	σ	2.45	8.45
Surface charge	σ_e	-10–0	-10–0
Viscosities	$[\mu_1, \mu_2]$	[1.0;1.0]	[1.0;1.0]
Densities	$[\rho_1, \rho_2]$	[10.;10.]	[10.;10.]
Relative permittivities	$[\epsilon_1, \epsilon_2]$	[1.0;1.0]	[1.0;1.0]
Solution energies	$[\beta_1^{\pm}, \beta_2^{\pm}]$	[4;1]	[4;1]
Ion mobilities	$[D_1^{\pm}, D_2^{\pm}]$	[0.0001;0.01]	[0.0001;0.01]
Inlet number density	$c_0^{\pm}$	2	2
Sheer velocity	u_{top}	0.2	–
Pressure difference	Δp	–	0–5–50

Table 3.1: The simulation parameters, both for the dead-end pore geometri and the pore throat set up. The superscript $\pm$ means of both the posetiv and negative ions.

Note that origo is set in the lower left corner. The initial phase field is also used to initialize the number densities in the following way:

$$c_i = 0.5(1 - \phi)c_0 \tag{3.3.2}$$

meaning that there will only be ions in the phase indicated with a II at the beginning of the simulations. The boundary and initial conditions for the pore throat Fig. 3.3.2 is rather similar to that of the dead-end pore, however, there are some differences. At the inlet and outlet, marked with a dashed line, we have prescribed a pressure boundary condition, setting the inlet pressure to $p = \Delta p$ and the outlet one to $p = 0$. The velocity field was set so there was no normal strain. The number-density at the in/outlet were set to be constant for both of the two ions and equal to the following value $c_i = c_0$ and the electric potential was grounded in both ends. On the channel wall itself, which is marked as the solid line black or blue depending on whether it is charged or not, we sat a no-slip condition on the velocity field, a no-flux conditions on the number-densities and a flux-condition on the electric potential to match the surface charge. Note that only the path where the wall is marked with blue have a non-vanishing surface charge. Finally, for the phase field, a non-flux and neutral contact angel were set on the wall boundaries, at the in/outlet it was set to $\phi = -1$ which is the value of the phase marked with a roman numeral II. The phase field was once again initialized with a tangent hyperbolic profile, this time defined as:

$$\phi = -2\left(\left(\tanh\left(\frac{x - (2/3L_x - 2R)}{\sqrt{2}\varepsilon}\right) - \tanh\left(\frac{x - (1/3L_x + 2R)}{\sqrt{2}\varepsilon}\right)\right) + 0.5\right) \tag{3.3.3}$$

and again origo is placed in the lower left corner and the initial number densities is given by Eq. (3.3.2).

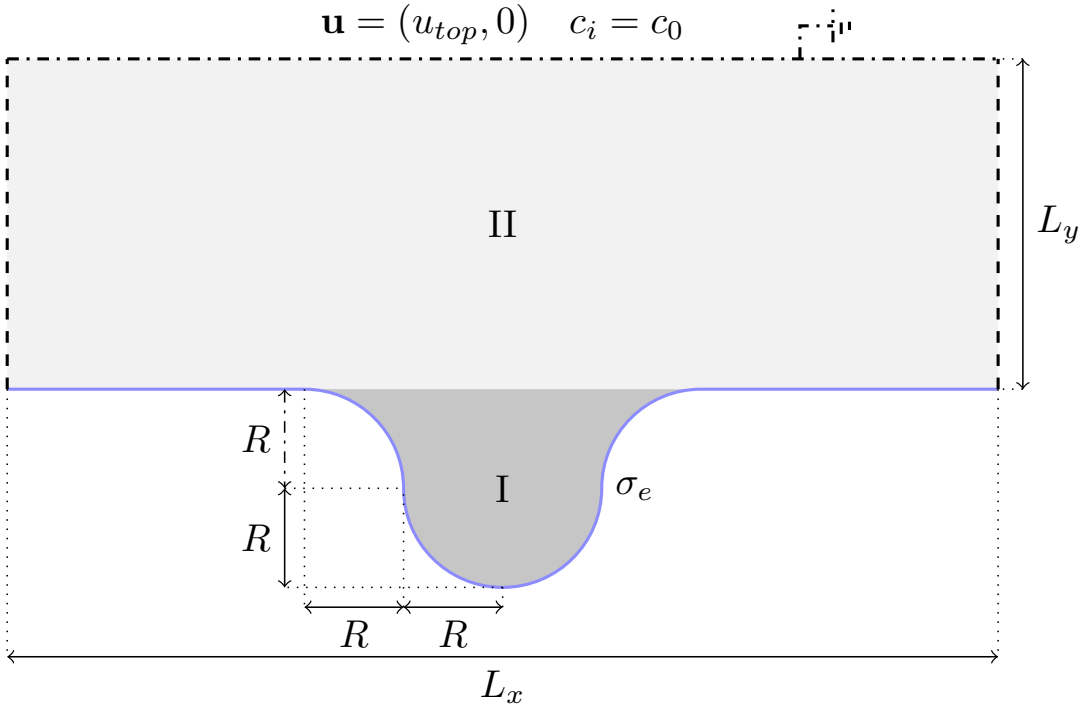

Figure 3.3.1: A semantic of the "dead-end pore" geometry, with the appropriate boundary conditions for the problem and specified initial conditions for phase field. The geometry is specified by the two lengths L_x, L_y, and the radius R used to define the dead-end pore in the center of in the channel by a circle and a circler soothed inlet. The roman numerals indicated the phase, along with the tone of gray, the darker one is the oil-like phase (I) and the light on is the water like phase (II).

3.4 Numerical Results

In the two geometries discussed in the section above we ran simulations under the parameters given in Table 3.2, and in order to see the difference we ran them both with a surface charge; $\sigma_e = -10$ and without; i.e. $\sigma_e = 0$. Furthermore we ran the pore throat with different pressure differences. In the following subsections, we will present the results of those simulations but as paper printings do not support any video format it will be hard to give a detailed account of the completed dynamics, however, one can find GIFs[5] of the simulations on *Bernaise* git repository: https://github.com/gautelinga/BERNAISE.

It should be noted that the computational resource used was our in-house server with 2 64 bit CPUs, 28 cores ad 2.6 GHz and 512 Gb of RAM, which ran all of the simulation in about 5 hours So the choice of simulation resource was mainly based on convenience rather than necessity as the simulation presented here could without problems have been run on a modern workstation in a day or two.

3.4.1 Visualization

We have visualized the simulation in two different ways in order to illustrate the numerical experiments, each having their advantages. For the dead-end pore, we have made plots with the *Bernaise*

[5]Graphics Interchange Format

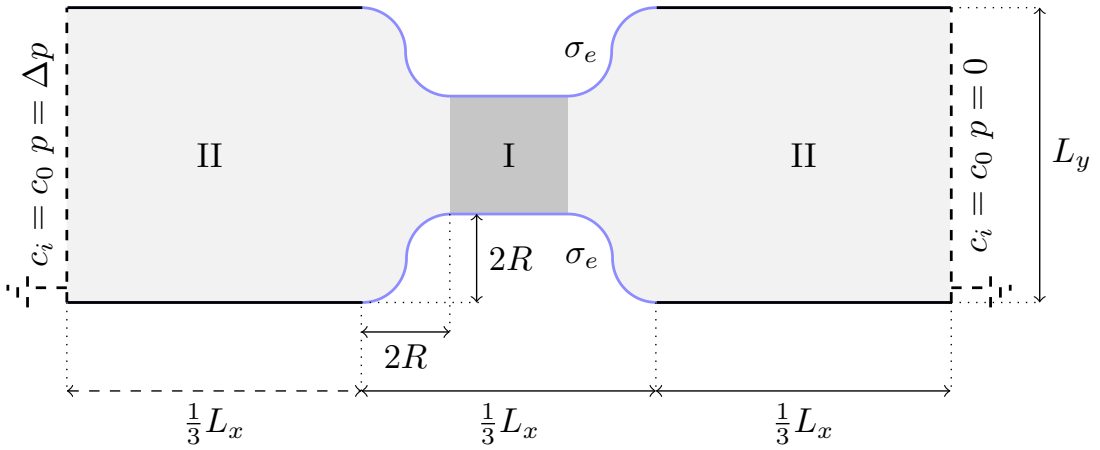

Figure 3.3.2: The schematic of the pore throat with an oil-like-plug in the narrowed region. The narrowing of the pore is done with two arcs both with a radius of R as indicated on the drawing. The boundary conditions are indicated on the schematic but one should refer to text for a precise description.

native GIF making tool found `"postprocess.py"`. This produces automatically a GIF from the simulation data where the ”water” phase shows the charge-density in a with a color map going from blue for negative to red for positive and all scaled to the maximum density in the time series. The ”oil” phase forms in this mapping a black region for the level set of the phase field larger than 0. The level set visualization to make each phase appear defined in a more clear way than what is actually the case, which means that one might not realize phase traces that are left due to under-resolved time step.

For the single pore we have used Paraview[6] to make the plots and thereafter stitched them together to form a video, where one can choose a more smooth transition that the *Bernaise* native one. This visualizes the diffused interface better, however, it is way more time consuming to produce the plots and it tends to be more useful as a previewing tool, especially if the simulation is well resolved in time and space.

3.4.2 Dead-end Pore

The simulation of the dead-end pore was carried out to get preliminary confirmation of the hypotheses from Section 3.2.1, that electrowetting could be responsible for the expelling. Those simulation have also been used for the parer in Appendix B so the figures have a overlap. We wanted to see the differences of having electrostatic effects or not, hence we present pictures of the simulation at different times for both cases in Fig. 3.4.1. The left column Figs. 3.4.1a, 3.4.1c and 3.4.1e is for the vanishing surface charge and the right column is for a surface charge of $\sigma_e = -10$. For the none-charge case not much happen between the frames that we have shown, in fact, the main difference is the numerical noise of the total charge and it is due to errors of machine precision. Of course there were some initial dynamics of oil-like-plug where it was distorted so it’s interface compile with a neutral contact angel and the shear flow, however, this mainly happens before the first frame presented.

A rather different behavior is seen in the right column Figs. 3.4.1b, 3.4.1d and 3.4.1f where a surface charge was applied. Here we see first two tongues are intruding on both sides of the droplet, while the oil-like fluid is pushed out in the center of the dead-end pore. The process is continued in the

[6]https://www.paraview.org/

second frame and finalized in the third frame with the complete release of the droplet due to the two tongues meeting in the middle of the dead-end severing the contact. Hence we see that the effects of the surface charge mean that the ”water”-phase on larger scales behaves like it is completely wetting even when we enforced a neural contact angel. To exemplify this effect furthermore we have carried out a similar simulation in the next section for a pore throat filled with oil-like fluid, but with a pressure difference applied.

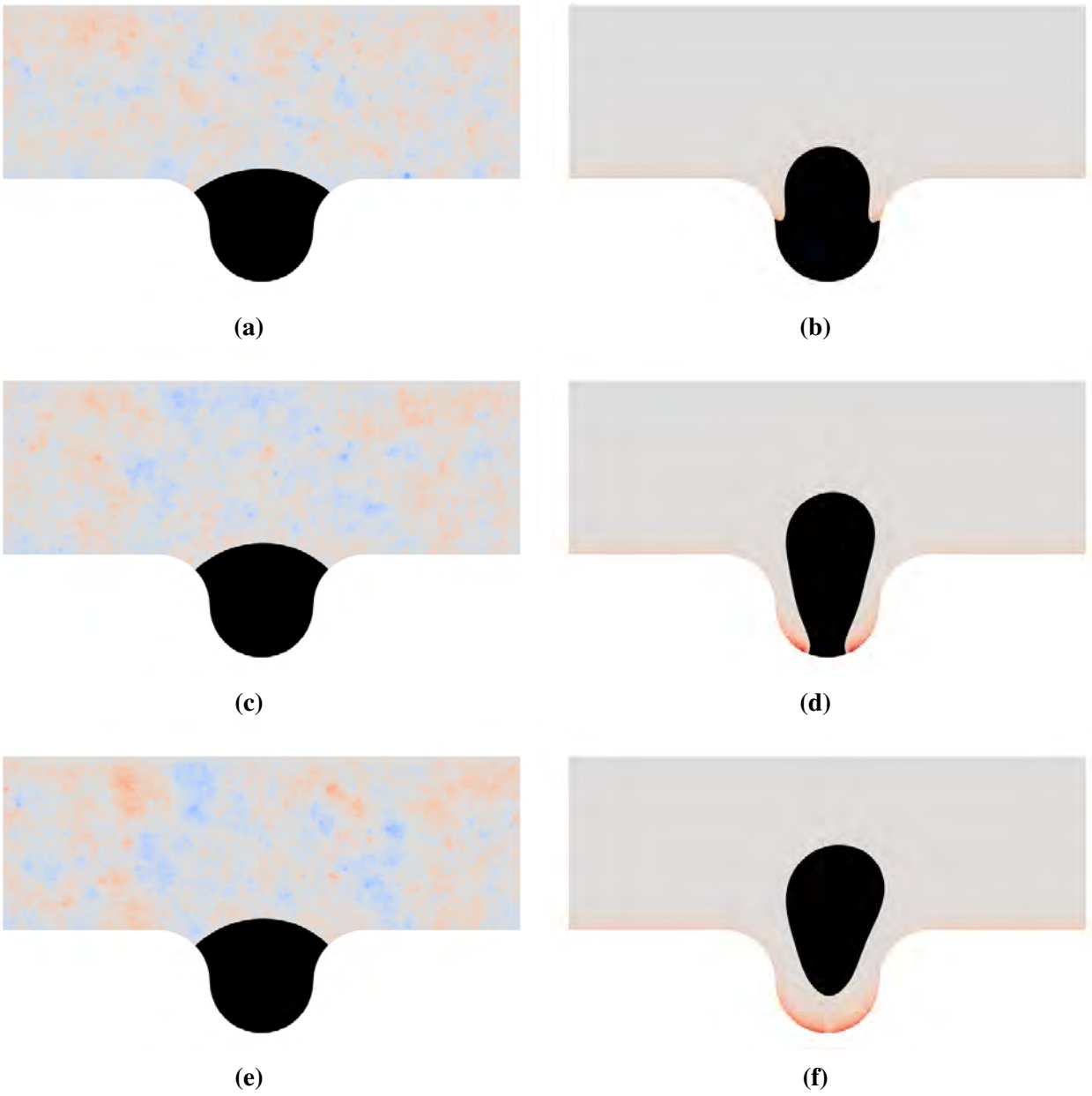

Figure 3.4.1: The simulation of the dead-end pore under a shear flow, the left column the surface charge is vanishing and to the right, we have $\sigma_e = -10$. The first row is for $t = 300dt$, the second is for $t = 600dt$, and finally the third row is $t = 900dt$.

Name	Simulation Parameters	"Dead-end"	"Throat"
Length	L_x	3.0	6.0
Hight	L_y	1.0	2.0
Total Time	t	20	20
Radius	R	0.3	0.3
Time step	dt	0.01	0.02
Resolution	res	120	120
Interface thickness	ε	0.02	0.02
Phase field mobility	M_0	$2.5 \cdot 10^{-6}$	$2.5 \cdot 10^{-6}$
Surface tension	σ	2.45	8.45
Surface charge	σ_e	-10–0	-10–0
Viscosities	$[\mu_1, \mu_2]$	[1.0;1.0]	[1.0;1.0]
Densities	$[\rho_1, \rho_2]$	[10.;10.]	[10.;10.]
Relative permittivities	$[\epsilon_1, \epsilon_2]$	[1.0;1.0]	[1.0;1.0]
Solution energies	$[\beta_1^{\pm}, \beta_2^{\pm}]$	[4;1]	[4;1]
Ion mobilities	$[D_1^{\pm}, D_2^{\pm}]$	[0.0001;0.01]	[0.0001;0.01]
Inlet number density	$c_0^{\pm}$	2	2
Sheer velocity	u_{top}	0.2	–
Pressure difference	Δp	–	0–5–50

Table 3.2: The simulation parameters, both for the dead-end pore geometri and the pore throat set up. The superscript $\pm$ means of both the posetiv and negative ions.

3.4.3 Pore Throat

As mentioned earlier we have simulated the pore throat not only with and without surface charge but also for different pressure difference over the pore to see the effect of driving the system. The results are shown grouped by the different pressures in Figs. 3.3.1, 3.4.3 and 3.4.4 for $\Delta p = 0$, $\Delta p = 5$, $\Delta p = 50$ respectively.

The simulation where $\Delta p = 0$ we see in four different time frames. In the left column (Figs. 3.4.2a, 3.4.2c, 3.4.2e and 3.4.2g) the surface charge was vanishing. Due to the vanishing pressure, surface charge and neutral contact angel we see that nothing happens to the oil-like-plug in the throat, as the walls are perpendicular to the contact line between the oil-like fluid and "water-like fluid. However in the right column (Figs. 3.4.2b, 3.4.2d, 3.4.2f and 3.4.2h) we see the oil-like fluid is excludet from the throat. This happens similar to the case of the dead-end pore by tongues intruding along the charge wall due to the forming of electric double layers in the water-like-phase. In the last two frames of the simulation, one sees as expected a "spontaneous"–symmetry breaking, where the droplet is expelled to the left side, we believe the underlying perturbation for this particular case is an underlying asymmetry in the mesh.

The simulation where $\Delta p = 5$ we again have shown in four different time frames, and once again the left column (Figs. 3.4.3a, 3.4.3c, 3.4.3e and 3.4.3g) is for the vanishing surface charge. This time, however, we see some difference from the initial state, The oil-like-plug is deformed in the outlet until Poisson pressure balances the pressure difference over the pore. This means that no dynamics are present after the deformation of the droplet has taken place and it is never expelled from the pore. In the right column (Figs. 3.4.3b, 3.4.3d, 3.4.3f and 3.4.3h) we see that the dynamic of the expelling does not change that much from the case with no pressure difference. Off course, the droplet is expelled

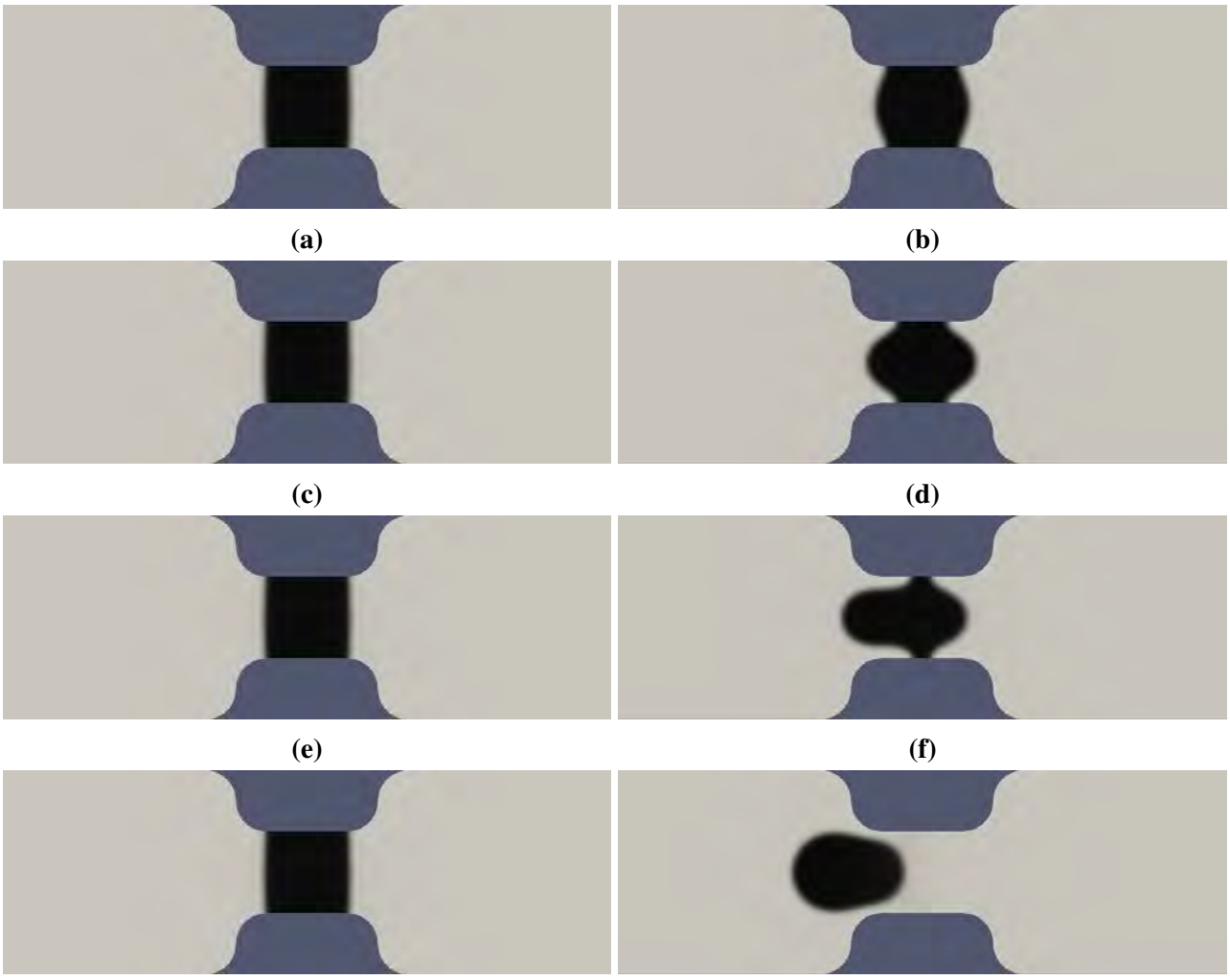

Figure 3.4.2: The simulation of the pore throat with a pressure difference $\Delta p = 0$, the left column the surface charge is vanishing and in the right we have $\sigma_e = -10$. The first row is for $t = 250dt$, the second is for $t = 500dt$, the third $t = 750dt$ and finally the fourth row is for $t = 1000dt$.

to the right side due to the applied pressure difference, and the "water" tongues on the left side of the throat are not as pronounced. Note that the time scale of the expelling of the droplet is more or less the same for both $\Delta p = 0$ and $\Delta p = 5$, meaning that it must be controlled by the electric forces in this regime.

The last simulation was for a pressure difference of $\Delta p = 50$ and here as well we show the simulation without surface charge in the left column (Figs. 3.4.4a, 3.4.4c, 3.4.4e and 3.4.4g). Note that in this case the time step might be on the lower end of what was needed in order to resolve the dynamics as there is a rather large leaking of the oil-like-phase in Figs. 3.4.4g and 3.4.4h. Here we see that as the pressure is so large that the oil-like-plug is blowns out of the throat, as the Poisson pressure cannot balance the applied pressure. The plug is an eventually ripped apart. After the rapture of the oil-like-plug it is not released from the wall but is still attached a the end of the simulation. For longer simulations it would presumably stay there, but maybe it would migrate along the wall towards the outlet. For the right column (Figs. 3.4.4b, 3.4.4d, 3.4.4f and 3.4.4h) we see that the dynamics in the initial two frames is to a large extend similar to it's no charge counterpart. However one begins to see a difference in the dynamics due to the electric forces, as the motion seem slightly dampened and

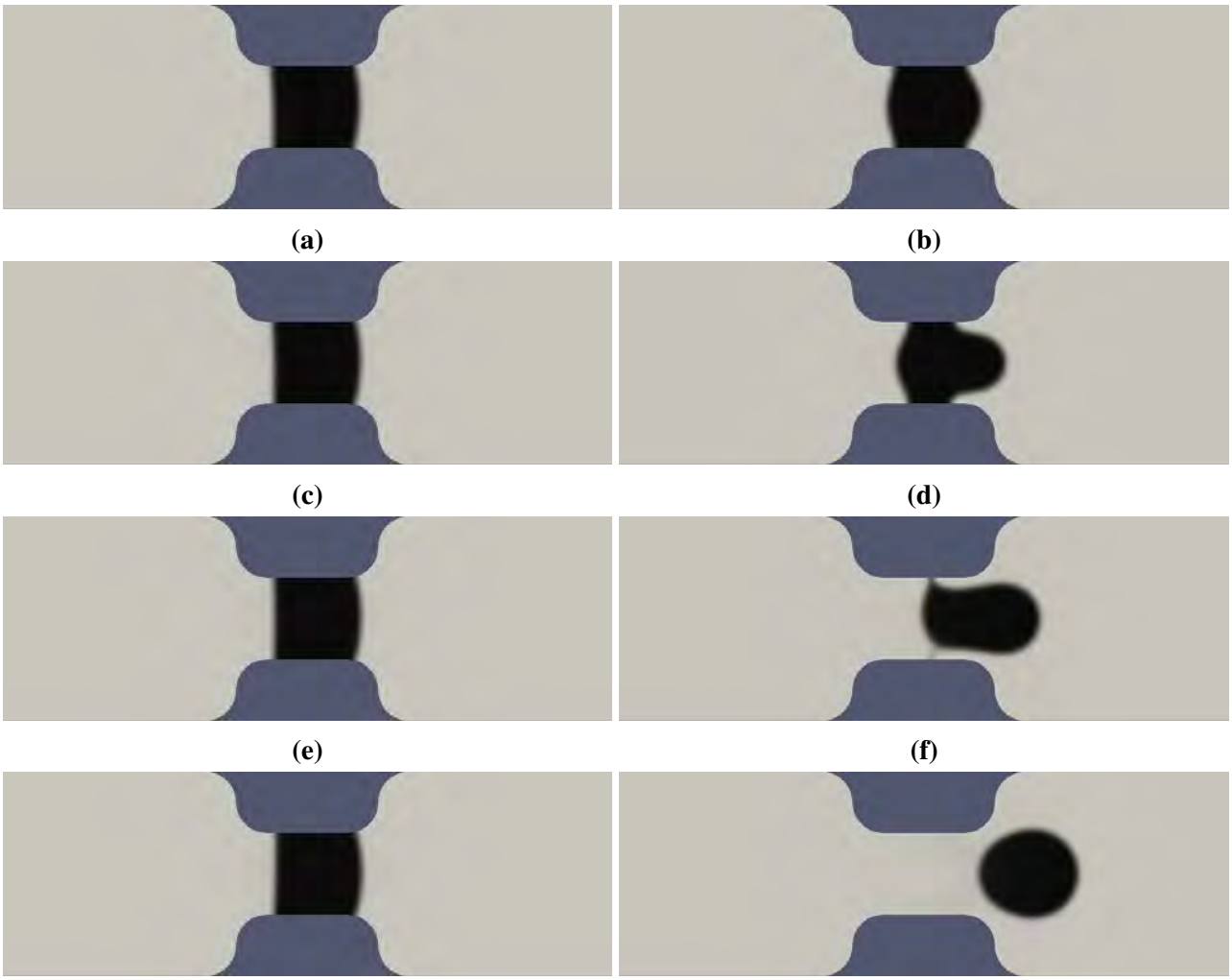

Figure 3.4.3: The simulation of the pore throat with a pressure difference $\Delta p = 5$, the left column the surface charge is vanishing and in the right we have $\sigma_e = -10$. The first row is for $t = 250dt$, the second is for $t = 500dt$, the third $t = 750dt$ and finally the fourth row is for $t = 1000dt$.

that the oil-like fluid is eventually released from the wall in. Hence even if the flow is dominated by enforced pressure differences the local electric forces can still change the macroscopic dynamics of the fluids.

3.5 Future Prospects

Off course, the simulations done in the former section was preliminary studies, and one can find many contexts where electric effects could also play a role. But to stick to the contexts already addressed in the *Bernaise* paper and in this chapter, an obvious next step would be to introduce an axial symmetric code for the problem to probe some 3-dimensional effects . Such a step would allow to extend the study of electrowetting to the case of a 3 dimensional droplet and eventually map out the phase diagram found by Monroe et al. [50] by numerical means. Another use of the numerical framework would be to the study of intrusion would be to simulate Washburn regime capillary intrusion driven by either surface potential or a surface charge. However, for the surface charge case there is a challenge as the

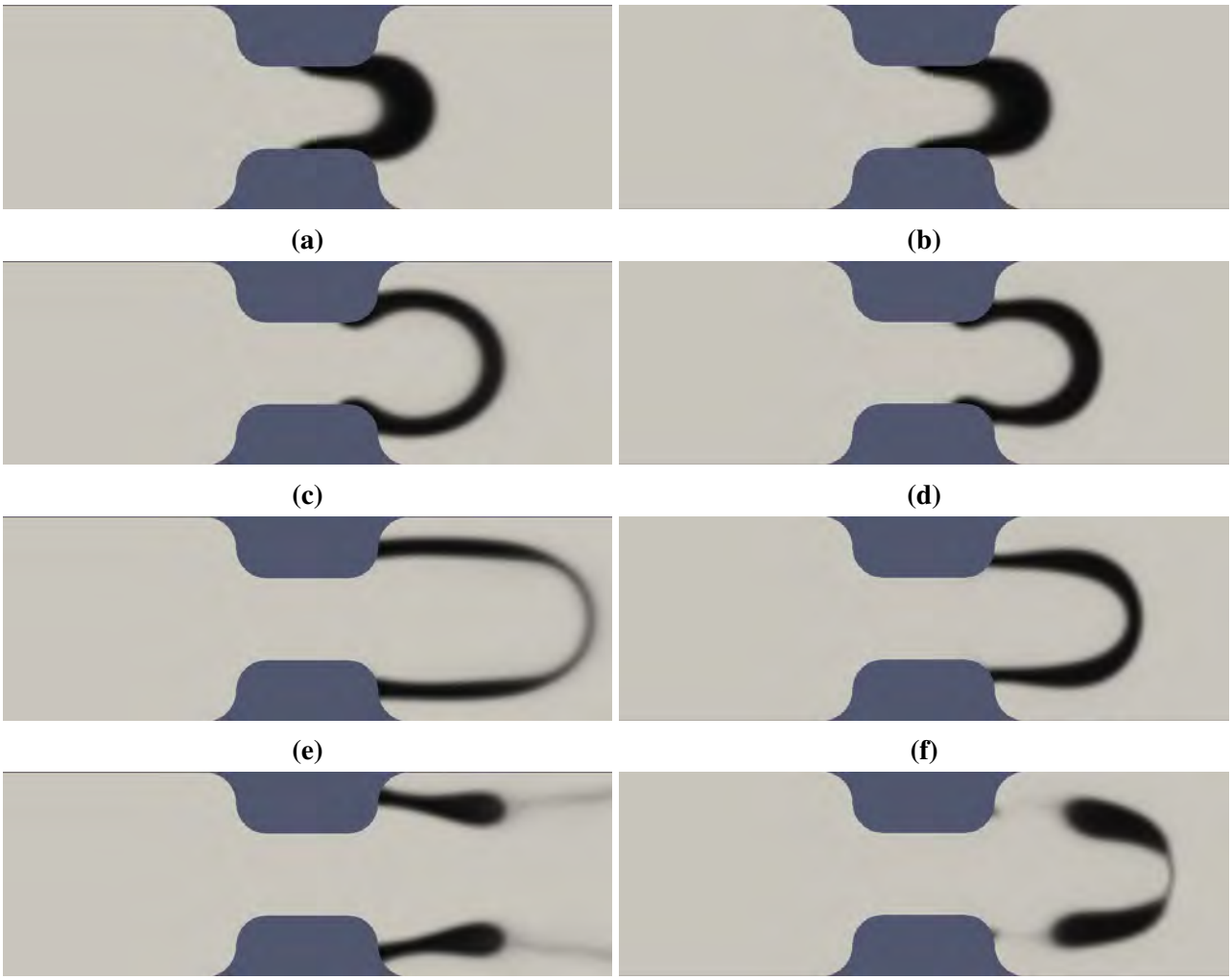

Figure 3.4.4: The simulation of the pore throat with a pressure difference $\Delta p = 50$, the left column the surface charge is vanishing and in the right, we have $\sigma_e = -10$. The first row is for $t = 100dt$, the second is for $t = 200dt$, the third $t = 300dt$ and finally the fourth row is for $t = 400dt$.

electric field depends extensively on the surface area if no screening occurred. So if the local intrusion should be independent of the system size one would need to screen the electric field in both phases just with different Debye lengths. Such an intrusion set up could be extended to even more complicated geometries like a 2-dimensional porous media, and the change of interface dynamics could be studied. Finally, one could consider extending the code to 3-dimensions to expand the studies of porous media further. But one would need to invest time in making the solvers fully iterative in order to manage the larger demand on computational resources required by the increase in system size.

Chapter 4

Conclusion

From numerical simulations, we have studied qualitatively and quantitatively the electrohydrodynamics in complex geometries. In the case of single-phase flow, we show in a model fracture aperture that electrohydrodynamics can cause significant flow reduction and enhanced flow channeling relative to regular pressure driven flow. The work is included in the manuscripts in the Appendices A and C. Our results may find application in natural and industrial contexts where electrolyte solutions flow though fractures and pores. Further studies in larger complex geometries as well as systems with higher ion-number densities would be natural next steps of our work.

In the case of two-phase flow, we have simulated electrowetting. We found that in an oil-water system, that the oil phase was much easier expelled when there were ions present in the aqueous phase. Furthermore, we observed that the apparent contact angle could be changed significantly, in fact so much that the water phase effectively became fully wetting. This observation have been the basis for more detailed studies of the electric-potential effect on electrowetting for at droplet, included in the manuscript found in Appendix B. The simulation framework used in the two-phase flow lead was presented in a manuscript included in Appendix D. Future work will extend the numerical code to three-dimensions and possible include further quantitative analysis of oil extraction in porous media.

Bibliography

[1] Helmut Abels, Harald Garcke, and Günther Grün. Thermodynamically consistent, frame indifferent diffuse interface models for incompressible two-phase flows with different densities. *Mathematical Models and Methods in Applied Sciences*, 22(03):1150013, 2012.

[2] Martin S. Alnæs. *UFL: a Finite Element Form Language*, chapter 17. Springer, 2012.

[3] Martin S. Alnæs, Jan Blechta, Johan Hake, August Johansson, Benjamin Kehlet, Anders Logg, Chris Richardson, Johannes Ring, Marie E. Rognes, and Garth N. Wells. The fenics project version 1.5. *Archive of Numerical Software*, 3(100), 2015.

[4] Martin S. Alnæs, Anders Logg, and Kent-Andre Mardal. *UFC: a Finite Element Code Generation Interface*, chapter 16. Springer, 2012.

[5] Martin S. Alnæs, Anders Logg, Kent-Andre Mardal, Ola Skavhaug, and Hans Petter Langtangen. Unified framework for finite element assembly. *International Journal of Computational Science and Engineering*, 4(4):231–244, 2009.

[6] Martin S. Alnæs, Anders Logg, Kristian B. Ølgaard, Marie E. Rognes, and Garth N. Wells. Unified form language: A domain-specific language for weak formulations of partial differential equations. *ACM Transactions on Mathematical Software*, 40(2), 2014.

[7] Alexander Altland and Ben D Simons. *Condensed matter field theory*. Cambridge University Press, 2010.

[8] Daniel M Anderson, Geoffrey B McFadden, and Adam A Wheeler. Diffuse-interface methods in fluid mechanics. *Annual review of fluid mechanics*, 30(1):139–165, 1998.

[9] Claude Bardos, François Golse, and David Levermore. Fluid dynamic limits of kinetic equations. i. formal derivations. *Journal of statistical physics*, 63(1):323–344, 1991.

[10] David Beamish and RJ Peart. Electrokinetic geophysics a review. *Terra Nova*, 10(1):48–55, 1998.

[11] G Beni and S Hackwood. Electro-wetting displays. *Applied Physics Letters*, 38(4):207–209, 1981.

[12] G Beni and MA Tenan. Dynamics of electrowetting displays. *Journal of applied physics*, 52(10):6011–6015, 1981.

[13] Anders Brask, Goran Goranović, Mads Jakob Jensen, and Henrik Bruus. A novel electro-osmotic pump design for nonconducting liquids: theoretical analysis of flow rate–pressure characteristics and stability. *Journal of Micromechanics and Microengineering*, 15(4):883, 2005.

[14] Timothy R Brumleve and Richard P Buck. Numerical solution of the nernst-planck and poisson equation system with applications to membrane electrochemistry and solid state physics. *Journal of Electroanalytical Chemistry and Interfacial Electrochemistry*, 90(1):1–31, 1978.

[15] Eduard Campillo-Funollet, G Grun, and Fabian Klingbeil. On modeling and simulation of electrokinetic phenomena in two-phase flow with general mass densities. *SIAM Journal on Applied Mathematics*, 72(6):1899–1925, 2012.

[16] Alfredo E Cardenas, Rob D Coalson, and Maria G Kurnikova. Three-dimensional poisson-nernst-planck theory studies: Influence of membrane electrostatics on gramicidin a channel conductance. *Biophysical Journal*, 79(1):80–93, 2000.

[17] Howard C Elman, David J Silvester, and Andrew J Wathen. *Finite elements and fast iterative solvers: with applications in incompressible fluid dynamics*. Numerical Mathematics & Scientific Computation, 2014.

[18] Misha Marie Gregersen, Mathias Bækbo Andersen, Gaurav Soni, Carl Meinhart, and Henrik Bruus. Numerical analysis of finite debye-length effects in induced-charge electro-osmosis. *Physical Review E*, 79(6):066316, 2009.

[19] Tue Hassenkam, Christian S Pedersen, K Dalby, Tor Austad, and Susan Louise Svane Stipp. Pore scale observation of low salinity effects on outcrop and oil reservoir sandstone. *Colloids and Surfaces A: Physicochemical and Engineering Aspects*, 390(1-3):179–188, 2011.

[20] Robert A Hayes and B Johan Feenstra. Video-speed electronic paper based on electrowetting. *Nature*, 425(6956):383, 2003.

[21] E Hilner, Martin Peter Andersson, Tue Hassenkam, Jesper Matthiesen, PA Salino, and Susan Louise Svane Stipp. The effect of ionic strength on oil adhesion in sandstone–the search for the low salinity mechanism. *Scientific reports*, 5:9933, 2015.

[22] Pierre C Hohenberg and Bertrand I Halperin. Theory of dynamic critical phenomena. *Reviews of Modern Physics*, 49(3):435, 1977.

[23] JL Jackel, S Hackwood, and G Beni. Electrowetting optical switch. *Applied Physics Letters*, 40(1):4–5, 1982.

[24] John David Jackson. *Classical electrodynamics*. Wiley, New York, NY, 3rd ed. edition, 1999.

[25] Robert C. Kirby. Algorithm 839: Fiat, a new paradigm for computing finite element basis functions. *ACM Transactions on Mathematical Software*, 30(4):502–516, 2004.

[26] Robert C. Kirby. *FIAT: Numerical Construction of Finite Element Basis Functions,*, chapter 13. Springer, 2012.

[27] Robert C. Kirby and Anders Logg. A compiler for variational forms. *ACM Transactions on Mathematical Software*, 32(3), 2006.

[28] John G Kirkwood. Theory of solutions of molecules containing widely separated charges with special application to zwitterions. *The Journal of Chemical Physics*, 2(7):351–361, 1934.

[29] Stein Kuiper and BHW Hendriks. Variable-focus liquid lens for miniature cameras. *Applied physics letters*, 85(7):1128–1130, 2004.

[30] Lev Davidovich Landau, JS Bell, MJ Kearsley, LP Pitaevskii, EM Lifshitz, and JB Sykes. *Electrodynamics of Continuous Media*, volume 8. elsevier, 2013.

[31] Lev Davidovich Landau and E. M. Lifshitz. *Statistical Physics 3rd Edition Part 1*, volume 5. Pergamon Press, 1980.

[32] Lev Davidovich Landau and E. M. Lifshitz. *Fluid Mechanics*, volume 6. elsevier, 1987.

[33] Hans Petter Langtangen, Kent-Andre Mardal, and Ragnar Winther. Numerical methods for incompressible viscous flow. *Advances in Water Resources*, 25(8):1125–1146, 2002.

[34] Benny Lautrup. *Physics of continuous matter: exotic and everyday phenomena in the macroscopic world*. CRC press, 2011.

[35] Choongyeop Lee, Laurent Joly, Alessandro Siria, Anne-Laure Biance, Remy Fulcrand, and Lyderic Bocquet. Large apparent electric size of solid-state nanopores due to spatially extended surface conduction. *Nano letters*, 12(8):4037–4044, 2012.

[36] Roland Lenormand, Eric Touboul, and Cesar Zarcone. Numerical models and experiments on immiscible displacements in porous media. *Journal of fluid mechanics*, 189:165–187, 1988.

[37] Gaute Linga, Asger Bolet, and Joachim Mathiesen, 2018. unpublished.

[38] Gabriel Lippmann. *Relations entre les phénomènes électriques et capillaires*. PhD thesis, Gauthier-Villars, 1875.

[39] Jinn-Liang Liu and Bob Eisenberg. Numerical methods for a poisson-nernst-planck-fermi model of biological ion channels. *Physical Review E*, 92(1):012711, 2015.

[40] Anders Logg, Kent-Andre Mardal, Garth N. Wells, et al. *Automated Solution of Differential Equations by the Finite Element Method*. Springer, 2012.

[41] Anders Logg, Kristian B. Ølgaard, Marie E. Rognes, and Garth N. Wells. *FFC: the FEniCS Form Compiler*, chapter 11. Springer, 2012.

[42] Anders Logg, Garth N. Wells, and Johan Hake. *DOLFIN: a C++/Python Finite Element Library*, chapter 10. Springer, 2012.

[43] J Lowengrub and L Truskinovsky. Quasi–incompressible cahn–hilliard fluids and topological transitions. In *Proceedings of the Royal Society of London A: Mathematical, Physical and Engineering Sciences*, volume 454, pages 2617–2654. The Royal Society, 1998.

[44] Ali Mansouri, Carl Scheuerman, Subir Bhattacharjee, Daniel Y Kwok, and Larry W Kostiuk. Transient streaming potential in a finite length microchannel. *Journal of Colloid and Interface Science*, 292(2):567–580, 2005.

[45] JA Manzanares, WD Murphy, S Mafe, and H Reiss. Numerical simulation of the nonequilibrium diffuse double layer in ion-exchange membranes. *The Journal of Physical Chemistry*, 97(32):8524–8530, 1993.

[46] ST Martner and NR Sparks. The electroseismic effect. *Geophysics*, 24(2):297–308, 1959.

[47] JR Melcher and GI Taylor. Electrohydrodynamics: a review of the role of interfacial shear stresses. *Annual review of fluid mechanics*, 1(1):111–146, 1969.

[48] Gregor Mitscha-Baude, Andreas Buttinger-Kreuzhuber, Gerhard Tulzer, and Clemens Heitzinger. Adaptive and iterative methods for simulations of nanopores with the pnp–stokes equations. *Journal of Computational Physics*, 338:452–476, 2017.

[49] Hitoshi Mizutani, Tsuneo Ishido, Takanobu Yokokura, and Shuhei Ohnishi. Electrokinetic phenomena associated with earthquakes. *Geophysical Research Letters*, 3(7):365–368, 1976.

[50] Charles W Monroe, Leonid I Daikhin, Michael Urbakh, and Alexei A Kornyshev. Electrowetting with electrolytes. *Physical review letters*, 97(13):136102, 2006.

[51] CW Monroe, LI Daikhin, M Urbakh, and AA Kornyshev. Principles of electrowetting with two immiscible electrolytic solutions. *Journal of Physics: Condensed Matter*, 18(10):2837, 2006.

[52] Frieder Mugele. Fluid dynamics: To merge or not to merge... *Nature*, 461(7262):356, 2009.

[53] Frieder Mugele and Jean-Christophe Baret. Electrowetting: from basics to applications. *Journal of Physics: Condensed Matter*, 17(28):R705, 2005.

[54] Frieder Mugele, Michel Duits, and Dirk Van den Ende. Electrowetting: a versatile tool for drop manipulation, generation, and characterization. *Advances in colloid and interface science*, 161(1-2):115–123, 2010.

[55] W. Nernst. Zur kinetik der in lösung befi ndlichen körper. *Zeitschrift für Physikalische Chemie*, (2):613–637, 1888.

[56] Chiara Neto, Drew R Evans, Elmar Bonaccurso, Hans-Jürgen Butt, and Vincent SJ Craig. Boundary slip in newtonian liquids: a review of experimental studies. *Reports on Progress in Physics*, 68(12):2859, 2005.

[57] Christoffer P Nielsen and Henrik Bruus. Transport-limited water splitting at ion-selective interfaces during concentration polarization. *Physical Review E*, 89(4):042405, 2014.

[58] Amaël Obliger, Marie Jardat, Daniel Coelho, Samir Bekri, and Benjamin Rotenberg. Pore network model of electrokinetic transport through charged porous media. *Physical Review E*, 89(4):043013, 2014.

[59] Maxim A Olshanskii and Yuri V Vassilevski. Pressure schur complement preconditioners for the discrete oseen problem. *SIAM Journal on Scientific Computing*, 29(6):2686–2704, 2007.

[60] M. Planck. Uber die erregung von elektricität und wärme in elektrolyten. *Annalen der Physik*, 1890a(39):161–186, 1890.

[61] Steve R Pride and FD Morgan. Electrokinetic dissipation induced by seismic waves. *Geophysics*, 56(7):914–925, 1991.

[62] A RezaeiDoust, T Puntervold, S Strand, and T Austad. Smart water as wettability modifier in carbonate and sandstone: A discussion of similarities/differences in the chemical mechanisms. *Energy & fuels*, 23(9):4479–4485, 2009.

[63] CL Rice and R_ Whitehead. Electrokinetic flow in a narrow cylindrical capillary. *The Journal of Physical Chemistry*, 69(11):4017–4024, 1965.

[64] WD Ristenpart, JC Bird, A Belmonte, F Dollar, and HA Stone. Non-coalescence of oppositely charged drops. *Nature*, 461(7262):377, 2009.

[65] Yousef Saad. *Iterative methods for sparse linear systems*, volume 82. siam, 2003.

[66] Bjornar Sandnes, EG Flekkøy, HA Knudsen, KJ Måløy, and H See. Patterns and flow in frictional fluid dynamics. *Nature communications*, 2:288, 2011.

[67] Ory Schnitzer and Ehud Yariv. The taylor–melcher leaky dielectric model as a macroscale electrokinetic description. *Journal of Fluid Mechanics*, 773:1–33, 2015.

[68] Reto B Schoch, Jongyoon Han, and Philippe Renaud. Transport phenomena in nanofluidics. *Reviews of modern physics*, 80(3):839, 2008.

[69] Jonathan Richard Shewchuk. Triangle: Engineering a 2D Quality Mesh Generator and Delaunay Triangulator. In Ming C. Lin and Dinesh Manocha, editors, *Applied Computational Geometry: Towards Geometric Engineering*, volume 1148 of *Lecture Notes in Computer Science*, pages 203–222. Springer-Verlag, 1996. From the First ACM Workshop on Applied Computational Geometry.

[70] Hang Si. Tetgen, a delaunay-based quality tetrahedral mesh generator. *ACM Trans. Math. Softw.*, 41(2):11:1–11:36, 2015.

[71] Alessandro Siria, Marie-Laure Bocquet, and Lydéric Bocquet. New avenues for the large-scale harvesting of blue energy. *Nature Reviews Chemistry*, 1(11):0091, 2017.

[72] Todd M Squires and Stephen R Quake. Microfluidics: Fluid physics at the nanoliter scale. *Reviews of modern physics*, 77(3):977, 2005.

[73] Geoffrey Taylor. Studies in electrohydrodynamics. i. the circulation produced in a drop by electrical field. *Proceedings of the Royal Society of London. Series A. Mathematical and Physical Sciences*, 291(1425):159–166, 1966.

[74] Luong Duy Thanh and Rudolf Sprik. Permeability dependence of streaming potential coefficient in porous media. *Geophysical Prospecting*, 64(3):714–725, 2016.

[75] AH Thompson and GA Gist. Geophysical applications of electrokinetic conversion. *The leading edge*, 12(12):1169–1173, 1993.

[76] RR Thompson. The seismic electric effect. *Geophysics*, 1(3):327–335, 1936.

[77] Djebbar Tiab and Erle C Donaldson. *Petrophysics: theory and practice of measuring reservoir rock and fluid transport properties*. Gulf professional publishing, 2015.

[78] P. Debye u. E. Hückel. Zur theorie der elektrolyte. *Physikalische Zeitschrift*, 24(9):185–206, 1923.

[79] Evert Johannes Willem Verwey and Jan Theodoor Gerard Overbeek. *Theory of the stability of lyophobic colloids*. Elsevier, 1948.

[80] Ivan Vlassiouk, Sergei Smirnov, and Zuzanna Siwy. Nanofluidic ionic diodes. comparison of analytical and numerical solutions. *Acs Nano*, 2(8):1589–1602, 2008.

[81] Marian Ritter von Smolan Smoluchowski. Contribution à la théorie de l'endosmose électrique et de quelques phénomènes corrélatifs. *Bull. Int. Acad. Sci. Cracovie.*, 184.:403–420, 1903.

[82] Marian Ritter von Smolan Smoluchowski. "the thery of electrical caraphoresis and surface conduction". *Physikalische Zeitschrift*, (6):756–780, 1905.

[83] Shawn W Walker, Benjamin Shapiro, and Ricardo H Nochetto. Electrowetting with contact line pinning: Computational modeling and comparisons with experiments. *Physics of Fluids*, 21(10):102103, 2009.

[84] Augustus D Waller. A demonstration on man of electromotive changes accompanying the heart's beat. *The Journal of physiology*, 8(5):229–234, 1887.

[85] Qingzhen Yang, Ben Q Li, and Yucheng Ding. 3d phase field modeling of electrohydrodynamic multiphase flows. *International Journal of Multiphase Flow*, 57:1–9, 2013.

[86] Qingzhen Yang, Ben Q Li, Jinyou Shao, and Yucheng Ding. A phase field numerical study of 3d bubble rising in viscous fluids under an electric field. *International Journal of Heat and Mass Transfer*, 78:820–829, 2014.

[87] Hiroaki Yoshida, Tomoyuki Kinjo, and Hitoshi Washizu. Coupled lattice boltzmann method for simulating electrokinetic flows: A localized scheme for the nernst–plank model. *Communications in Nonlinear Science and Numerical Simulation*, 19(10):3570–3590, 2014.

Appendix A

Electrohydrodynamics channeling effects in narrow fractures and pores

The paper “Electrohydrodynamics channeling effects in narrow fractures and pores” published in American Physical Society’s Physical Review E followed by its supplementary-material.

Appendix B

Phase-field modelling of dynamic electrowetting with electrolytes

A paper submitted for review to Physical Review E with title: “Phase-field modelling of dynamic electrowetting with electrolytes”

Appendix C

Decoupled energy-stable schemes for transient electrohydrodynamic flow

A draft for a paper with the working title: “Decoupled energy-stable schemes for transient electrohydrodynamic flow”, Note that section 4.3 is derived from the supplementary-material from the paper found in Appendix A and is not in its final from, hence it is very similar.

Appendix D

Bernaise: A flexible framework for simulating two-phase electrohydrodynamic flows in complex domains

A draft for a paper with the working title: “Bernaise: A flexible and robust high-level phase-field solver for two-phase eletrohydrodynamics in complex domains”